



Science Arts & Métiers (SAM)

is an open access repository that collects the work of Arts et Métiers Institute of Technology researchers and makes it freely available over the web where possible.

This is an author-deposited version published in: <https://sam.ensam.eu>
Handle ID: <http://hdl.handle.net/10985/19435>

To cite this version :

Bin JIA, Alexis RUSINEK, Richard BERNIER, Slim BAHI, Paul WOOD, Raphaël PESCI - A novel technique for dynamic shear testing of bulk metals with application to 304 austenitic stainless steel - International Journal of Solids and Structures - Vol. 204-205, p.153-171 - 2020

Any correspondence concerning this service should be sent to the repository

Administrator : scienceouverte@ensam.eu



A novel technique for dynamic shear testing of bulk metals with application to 304 austenitic stainless steel

B. Jia^{a,b,*}, A. Rusinek^{c,d,e}, R. Pesci^b, R. Bernier^c, S. Bahi^c, P. Wood^f

^a ENSAM-Arts et Métiers ParisTech, Laboratory of Design, Manufacturing and Control (LCFC), 57070 Metz, France

^b ENSAM-Arts et Métiers ParisTech, Laboratory of Microstructure Studies and Mechanics of Materials (LEM3), UMR CNRS 7239, 57078 Metz, France

^c Lorraine University, Laboratory of Microstructure Studies and Mechanics of Materials (LEM3), UMR CNRS 7239, 57078 Metz, France

^d Institute of Fundamental Technological Research, Ul. Pawinskiego 5B, 02-106 Warsaw, Poland

^e Chair of Excellence, Departamento de Ingeniería Mecánica, UC3M (Carlos III University, Madrid) Avda. de la Universidad 30, 28911 Leganés, Madrid, Spain

^f Institute for Innovation in Sustainable Engineering, College of Engineering and Technology, University of Derby, Quaker Way, Derby DE1 3HD, UK

A B S T R A C T

This paper describes a new single-shear specimen (SSS) and method to characterize the dynamic shear behavior of bulk metals using a traditional Split Hopkinson Pressure Bar (SHPB). By this method, the shear behavior of materials can be tested conveniently over a wide range of strain rates within 10^5 s^{-1} . This technique was applied to a 304 austenitic stainless steel (ASS) under shear strain rates from 0.001 s^{-1} to 38700 s^{-1} at room temperature. Based on finite element (FE) simulations, it was found that the deformation of the specimen shear zone was dominated by shear stress/strain components. Stress state parameters represented by stress triaxiality η and Lode angle parameter $\bar{\theta}$ were found very close to zero, indicating a deformation mode of simple shear. Besides, an obvious gap existed between the local deformation behavior in the specimen shear zone and the macroscopic stress-strain relations measured by the strain gauges on the SHPB bars. A correction coefficient method was adopted to extract the real shear behavior from the experimentally obtained force-displacement data. Through comparisons between the tested and simulated stress-strain curves, a good agreement was obtained.

1. Introduction

Dynamic shear deformation and failure is present in many engineering applications such as sheet metal forming and machining, car crashworthiness and ballistic impact (Arias et al., 2008; Børvik et al., 2002a, 2002b; Grytten et al., 2009). As a complement to the commonly used mechanical testing methods such as uniaxial tension and compression, shear testing has several advantages. First, the stress and strain in a well-designed shear specimen is uniform to higher plastic strain avoiding necking instability which develops in a tension test and the radial inertia and barreling that develops in a compression test. The shear stress-shear strain relation can be derived from the experimentally obtained force-displacement data conveniently (Rusinek and Klepaczko, 2001; Xu et al., 2017). Second, the low stress triaxiality in a well designed shear specimen suppresses damage initiation and propagation (Bai and Wierzbicki, 2008; Bao and Wierzbicki, 2004) to enable characterization of a material at large plastic strain (Dorogoy et al., 2015;

Dorogoy and Rittel, 2017; Rittel et al., 2002). Third, the thickness of the specimen shear zone can be designed to be so small that very high strain rates in the range of 10^4 s^{-1} to 10^5 s^{-1} are possible (Klepaczko, 1994; Klepaczko et al., 1999; Xu et al., 2018; Zhou et al., 2017). In addition, stress state, represented by stress triaxiality η and Lode angle parameter $\bar{\theta}$, has been shown to influence the deformation and failure behavior of materials significantly (Bai and Wierzbicki, 2008; Dunand and Mohr, 2017; Fras et al., 2018). The effect of these two parameters on deformation and failure has been investigated using shear type specimens (Dorogoy et al., 2016, 2015; Francart et al., 2017).

Various specimen geometries have been proposed for dynamic shear testing. Among them, commonly used methods include the torsion specimens (Duffy et al., 1971), hat shape specimens (Meyers et al., 1986), double shear specimens (Campbell and Ferguson, 1970) and a newly developed shear-compression specimens (SCS) (Dorogoy et al., 2015; Rittel et al., 2002). Dynamic torsion testing using a modified Split Hopkinson Bar (SHB) device was first introduced by Duffy et al. (1971) to study the strain rate sensitivity of aluminum alloys. The torque was applied to a specimen through a flying wheel and by this method a maximum shear

strain rate of 800 s^{-1} was obtained. However, restricted by the maximum torque that can be stored in the incident bar, the strain rate regime in torsion testing is limited, even for specimens with very small shear zone dimensions (Rusinek and Klepaczko, 2001). Another attractive shear specimen design is called hat shape specimen, originally invented by Meyers et al. (1986). It is an axisymmetric specimen made of an upper hat part and a lower brim part. When a compressive force is applied to the top surface, the specimen shear zone deforms in a shear dominated stress state. Mostly, the diameter of the hat is larger than the brim and by modifying the relative dimensions of the two parts, a shear-compression instead of simple or pure shear stress state is obtained. However, during testing the shear direction and the volume of material involved in deformation is not constant such that the stress and strain components in the shear zone are not uniform. Hence, the method lacks precision in deriving the shear stress-shear strain relation of the material from the instrumented loadcell. Mostly, hat shape specimens tend to find application to microstructure characterization such as adiabatic shear banding (ASB) (Bronkhorst et al., 2006; Meyers et al., 2003; Peirs et al., 2010). By loading hat shape specimens on a conventional SHPB device and adopting a stop ring technique (Peirs et al., 2010), the evolution of shear localization over a wide range of strain rates and temperatures was studied. Double shear specimens were initially used by Campbell and Ferguson (1970) to study the strain rate and temperature sensitivity of mild steels. The original double shear specimens require a modified SHPB device. The central portion of the specimen is in contact with the input bar while the two edge supports are fixed to the output tube. With the relative displacement between the central part and two edge supports, the region between them develops shearing. Whilst testing a double shear specimen, the edge supports rotate and result in a non-uniform stress/strain field in the specimen. To solve this problem, much work has been done concerning specimen geometry optimization (Bonnet-Lebouvier and Klepaczko, 2002; Guo and Li, 2012; Harding and Huddart, 1980; Klepaczko, 1994; Klepaczko et al., 1999; Shi et al., 2014; Xu et al., 2017). Shi et al. (2014) studied a modified double shear specimen and clamping device to prevent specimen rotation. However, a problem with the clamping device is that it induces signal oscillations to the experimentally measured shear stress-shear strain relations. Furthermore, the lateral movement of specimen shear zone is constrained. At small strains, the influence is not obvious and the specimen may deform under simple shear; but at large strain, significant tension or compression components can be readily observed, resulting in a stress state in the specimen shear zone which deviates from simple shear (Guo and Li, 2012; Rusinek and Klepaczko, 2001; Shi et al., 2014). SCS specimen (Rittel et al., 2002) and its variants (Dorogoy et al., 2016, 2015) were originally developed to investigate the deformation behavior of materials at large strain (Dorogoy and Rittel, 2017). The SCS specimen is a cylinder with two slots machined at 45° to the longitudinal axis. By changing the angle between 0° and 90° , various stress states in the specimen shear zone was obtained and it was shown to be a practical method to study the stress state dependent deformation and failure behavior of materials (Duan et al., 2017; Francart et al., 2017). In addition to the four specimen types described, several other specimen geometries have also been developed. For example, based on the static specimen proposed by Bao and Wierzbicki (2004), Peirs et al. (2012, 2011) designed an eccentric notch specimen to study the deformation behavior of Ti6Al4V alloy under pure shear. Gray et al. (2016) proposed a compact forced simple shear specimen (CFSS) for microstructure characterization of 7039 aluminum alloy.

Aside from the wide variety of specimen geometries, the techniques used for dynamic shear testing varies. SHB device has been shown to be a most popular method for dynamic shear behavior

characterization. For example, hat shape specimens have been adopted in many studies (Bronkhorst et al., 2006; Meyers et al., 2003, 1986; Peirs et al., 2010) to investigate ASB formation using the conventional SHPB device. Split Hopkinson Pressure and Tension Bars were adopted by Rittel et al. (2002) and Dorogoy et al. (2016) to study large strain deformation behavior of several metallic materials using the specially designed SCS and STS specimens. Duffy et al. (1971), Marchand and Duffy (1988) studied ASB phenomenon in several alloys using a modified Split Hopkinson Torsion Bar and torsion specimens. In addition to the SHB device and its variants, a fast hydraulic machine was utilized by Rusinek and Klepaczko (2001) to determine the shear behavior of sheet steels under intermediate strain rates between 1 s^{-1} and 10^2 s^{-1} . The drop weight tower (Krüger et al., 2003; Meyer and Krüger, 2000) is another device that provides a larger amount of kinetic energy which has been shown to be suited to characterize high strength materials. Klepaczko (1994) developed a direct impact technique for shear testing at extremely high strain rates. Different from the conventional SHPB device, the shear specimen herein is impacted by a projectile directly. The projectile velocities were from 10 m/s to 200 m/s and corresponding shear strain rates were measured between 10^2 s^{-1} and 10^5 s^{-1} .

From the literature review, two questions are frequently encountered during dynamic shear testing of metallic materials. First, how to obtain a simple shear stress state in the specimen shear zone. Mechanical properties of materials are strongly influenced by the stress state. A simple shear stress state is particularly important for deformation and failure behavior study. However, limited by the specimen geometry design, a shear-compression or shear-tension stress state is often obtained (Dorogoy et al., 2016; Peirs et al., 2010; Rittel et al., 2002). Another question is how to derive the shear stress-shear strain relations of tested materials accurately. Dynamic shear specimens are commonly designed for two purposes: first, microstructure and failure behavior characterization such as the hat shape specimen and the CFSS specimen; second, quantitative shear stress-shear strain relations assessment. Compared to the former one, the latter is more difficult. If the stress state in the specimen shear zone is not simple shear or the distribution of stress/strain components is inhomogeneous (Merle and Zhao, 2004; Peirs et al., 2010; Xu et al., 2018), it is difficult to extract the real shear behavior from the globally obtained force-displacement data.

This paper describes a new shear specimen geometry for dynamic shear testing of bulk metals using the conventional SHPB. The new specimen and test method were used to investigate the shear behavior of 304 ASS and the experimental results are analyzed. In the fourth section, validation of the new shear specimen including force equilibrium state within the specimen, distribution of stress/strain components, stress state in specimen shear zone as well as the determination of shear stress-shear strain relations is performed by finite element analysis (FEA). Finally, the main conclusions are summarized in Section 5.

2. Methodology

2.1. The new shear specimen

For a well-designed shear specimen, the following requirements should be fulfilled:

- (1) A simple shear stress state in the specimen shear zone throughout the deformation process.

Stress state can be represented by stress triaxiality η and Lode angle parameter $\bar{\theta}$. The value of η is defined as the ratio of the

hydrostatic stress σ_m to the Von Mises stress $\bar{\sigma}$, while $\bar{\theta}$ is a function of the third invariant of the stress deviator and is used to distinguish the different stress states with the same η value in three dimensions.

$$\eta = \frac{\sigma_m}{\bar{\sigma}} = \frac{\sqrt{2}(\sigma_1 + \sigma_2 + \sigma_3)}{3\sqrt{(\sigma_1 - \sigma_2)^2 + (\sigma_2 - \sigma_3)^2 + (\sigma_3 - \sigma_1)^2}} \quad (1)$$

$$\bar{\theta} = \frac{(2\sigma_2 - \sigma_1 - \sigma_3)}{\sigma_1 - \sigma_3} \quad (2)$$

where σ_1 , σ_2 and σ_3 are the three principal stresses following the order $\sigma_1 \geq \sigma_2 \geq \sigma_3$. Values of η and $\bar{\theta}$ under several typical stress states are shown in Table 1.

- (2) Homogeneous stress/strain distribution in the specimen shear zone.
- (3) Simple relationship between the shear stress-shear strain curve and the experimentally obtained force-displacement data.

In order to adopt the shear specimen to the conventional SHPB device for dynamic shear testing, there are two further requirements:

- (4) Achieve a force equilibrium state within the specimen quickly.
- (5) Avoid the use of clamping system or screws to fix the specimen to the SHPB bars.

A single-shear specimen (SSS) which meets all the requirements is shown in Fig. 1. It is a cylinder with 17 mm height and 10 mm diameter: two "L" shaped symmetric slots are machined with the shear zone located between them. The specimen is designed to be one part without clamping grips, fixtures or screws as they may induce signal oscillation during propagation of the strain wave and corrupt the experimentally measured force-displacement data. The top and bottom surfaces of the specimen are in direct contact with the SHPB bars. The height and width of the specimen shear zone, represented by H and L , are designed to be 1.5 and 1.0 mm, respectively. The shear zone width L may be reduced to 0.3 mm to obtain higher strain rates. The corresponding specimen height also changes from 17 to 12 mm, so the force equilibrium state can be achieved within the specimen more quickly. In the region between the shear zone and the support elements, a radius of 0.1 mm is machined to reduce stress concentration.

The material studied is 304 ASS. It is a most widely used stainless steel due to its unique combination of elevated strength and high ductility. In manufacturing processes such as high speed machining, sheet metal forming and ballistic impact, the material is subjected to dynamic shear loading so that it is necessary to study the dynamic shear behavior.

2.2. The conventional SHPB device

Dynamic shear tests were conducted using a conventional SHPB device shown in Fig. 2. The device consists of a projectile, incident and transmitted bars and the SSS specimen is placed between the

two bars. All three parts of the SHPB device are made of Maraging steel with Young's modulus $E = 210$ GPa. When the projectile impacts the incident bar, an elastic compressive wave propagates along the incident bar. Upon reaching the incident bar/specimen interface, part of the signal is reflected back while the rest is transmitted to the specimen. After several reflections between the two end faces of the specimen, a force equilibrium state is achieved. After that, the signal propagates forward into the transmitted bar and is finally absorbed by a momentum trap. Two pairs of strain gauges in full bridge configuration were used to record the incident $\varepsilon_I(t)$, reflected $\varepsilon_R(t)$ and transmitted $\varepsilon_T(t)$ signals at a sampling rate of 100 MHz without filtering. The dispersion correction has been taken into consideration during the design of the SHPB device, where the ratio of incident radius to strain wave pulse r/λ is approximately 0.11. In this case, the strain wave signals are propagating down through the bars with negligible dispersions (Chen et al., 2009). Also, it was confirmed numerically with two strain gauges fixed respectively at the end face and the middle position of the SHPB bars that any dispersion indeed is negligible. Therefore, the experimentally obtained force and displacement at strain gauges are assumed to be the same as those at the specimen/bar interfaces. A high speed camera was used to record the deformation of the specimen at a frequency of 125,000 fps. To validate the measurement system the measured displacement-time data was compared to the result obtained from the strain gauges on the SHPB bars.

To obtain an accurate description of shear behavior a force equilibrium state within the SSS specimen is necessary. To evaluate the force equilibrium state on the two end faces of the specimen, Ravichandran and Subhash (1994) proposed a parameter, $R(t)$:

$$R(t) = \frac{|\Delta F(t)|}{F_{avg}(t)} = 2 \frac{|F_1(t) - F_2(t)|}{|F_1(t) + F_2(t)|} \quad (1)$$

where $F_1(t)$ and $F_2(t)$ are the two forces acting on each of the end faces of the specimen, respectively. They can be calculated as $F_1(t) = EA[\varepsilon_I(t) + \varepsilon_R(t)]$ and $F_2(t) = EA\varepsilon_T(t)$, E and A are Young's modulus and cross-sectional area of the SHPB bars, respectively. $\Delta F(t)$ and $F_{avg}(t)$ are respectively the difference and the average of the two forces. A force equilibrium state is achieved when $R(t)$ approaches zero.

On attaining a force equilibrium state within the specimen and based on the theory of one-dimensional wave propagation (Lindholm, 1964), the nominal shear strain rate $\dot{\gamma}_{nominal}$, nominal shear strain $\gamma_{nominal}$ and nominal shear stress $\tau_{nominal}$ are calculated by the following equations.

$$\dot{\gamma}(t)_{nominal} = \frac{C[\varepsilon_I(t) - \varepsilon_R(t) - \varepsilon_T(t)]}{L} \quad (2)$$

$$\gamma_{nominal}(t) = \int \dot{\gamma}_{nominal}(t) dt \quad (3)$$

$$\tau(t)_{nominal} = \frac{F_{avg}(t)}{A_s} \quad (4)$$

where C is the elastic wave speed traveling along the SHPB bars and A_s is the cross-sectional area of the specimen shear zone.

Table 1
Values of η and $\bar{\theta}$ under several typical stress states.

Stress state	Equi-biaxial compression	Uniaxial compression	Pure shear	Uniaxial tension	Equi-biaxial tension
η	-2/3	-1/3	0	1/3	2/3
$\bar{\theta}$	-1	1	0	-1	1

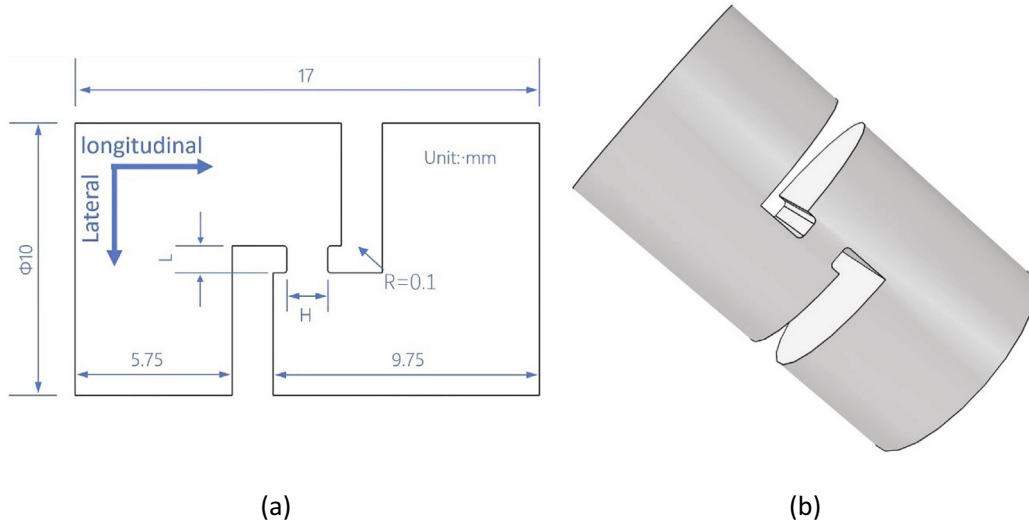


Fig. 1. Schematic diagram of the SSS specimen: (a) specimen dimensions and (b) 3D view.

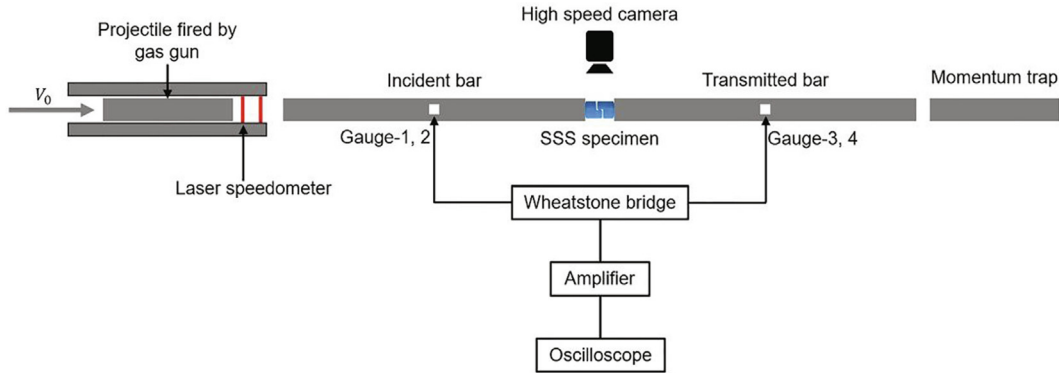


Fig. 2. Schematic diagram of the SHPB device.

3. Experimental results

Dynamic shear testing of 304 ASS under nominal shear strain rates ranging from 3000 s^{-1} to 45000 s^{-1} at room temperature was carried out using a conventional SHPB device. Specimens with different shear zone width L were used for various strain rate regimes: $L = 1 \text{ mm}$ for $\dot{\gamma}_{nominal} \leq 15000 \text{ s}^{-1}$; $L = 0.5 \text{ mm}$ for $15000 \text{ s}^{-1} < \dot{\gamma}_{nominal} \leq 30000 \text{ s}^{-1}$; $L = 0.3 \text{ mm}$ for $30000 \text{ s}^{-1} < \dot{\gamma}_{nominal}$. The typical strain wave signals measured from one test at $\dot{\gamma}_{nominal} = 6000 \text{ s}^{-1}$ are shown in Fig. 3. It is observed at $424 \mu\text{s}$, part of the incident signal begins to transfer into the SSS specimen, forming the transmitted signal. After that, the transmitted signal increases slightly while the reflected signal is almost constant. At $542 \mu\text{s}$, the transmitted signal starts to decrease, indicating damage initiation and growth in the specimen. Finally, the specimen fractures at $588 \mu\text{s}$ and at the same time the reflected signal reaches the maximum value.

Based on the strain wave signals in Fig. 3, the two forces acting on the end faces of the specimen, F_{in} and F_{out} , are calculated and shown in Fig. 4. In addition, parameter R is calculated according to Eq. 1 to validate the force equilibrium state. It is seen from Fig. 4 that at the initial stage of deformation, due to the non-perfect testing conditions, a strong signal oscillation is observed in F_{in} , and parameter R deviates obviously from zero. Hence, no force equilibrium state is achieved within the initial $45 \mu\text{s}$. After that, the two forces are reasonably close to each other and param-

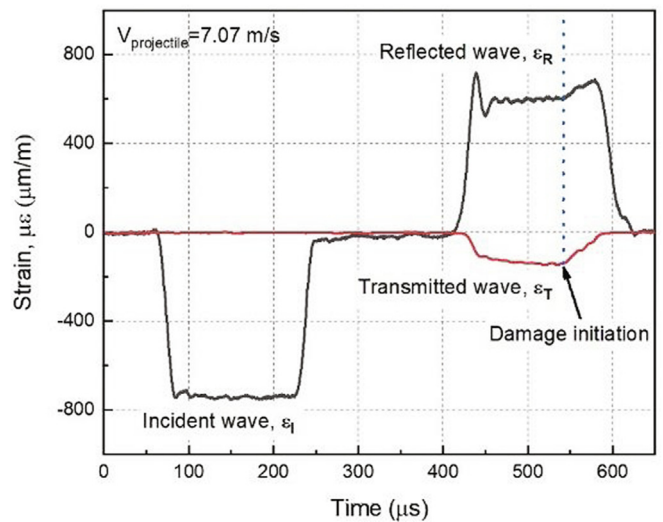


Fig. 3. Typical strain wave signals of SSS specimen measured by the SHPB technique.

eter R is always smaller than 0.1, indicating a force equilibrium state within the specimen. According to Eqs. (2)–(4), the nominal shear stress-nominal shear strain ($\tau_{nominal} - \gamma_{nominal}$) curve and the

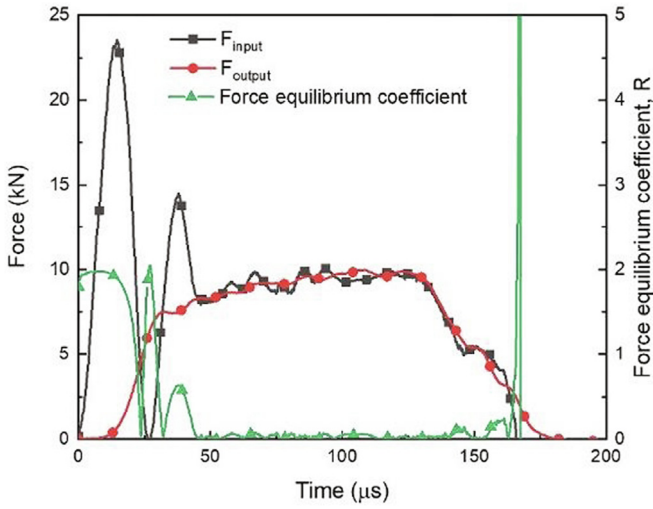


Fig. 4. Force-time curves at the bar/specimen interfaces and the corresponding force equilibrium coefficient R .

corresponding shear strain rate ($\dot{\gamma}_{nominal}$) are calculated and shown in Fig. 5. The yield stress of 304 ASS is measured to be 485 MPa. After the yield point, the flow stress increases continuously with an average strain hardening rate of 318 MPa/unit strain. Damage initiates at $\gamma_{nominal} = 0.66$ and then propagates quickly. Finally, specimen fracture is observed at $\gamma_{nominal} = 1.05$. During the whole plastic deformation process, the nominal shear strain rate keeps constant at $\dot{\gamma}_{nominal} = 6000 \text{ s}^{-1}$.

The deformation process of the SSS specimen was recorded by a high speed camera (Please see the supplementary data in Appendix B). It is observed that during deformation, the specimen neither rotates about the major axis nor experiences lateral displacement. Hence, the SSS specimen design without clamping system is demonstrated. From the video and software Tracker, the evolution of specimen displacement with time is analyzed and compared to the results obtained by the strain gauges, Fig. 6. The two curves almost coincide and the slight difference is attributed to the limited resolution capacity (312*260 pixels) of the high speed camera. What is more, from the strain gauges measurement, damage is initiated at $\gamma_{nominal} = 0.66$ while fracture is observed at $\gamma_{nominal} = 0.65$ from the camera measurement, suggesting high confidence in the specimen design, bar test system and measurements.

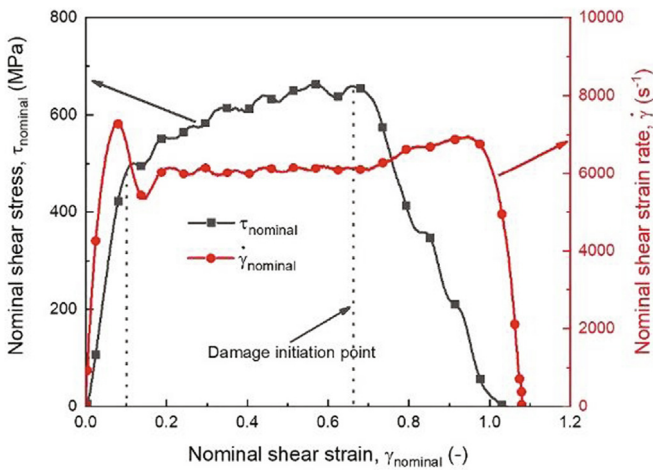


Fig. 5. Nominal shear stress-shear strain curve of the SSS specimen and the corresponding nominal shear strain rate.

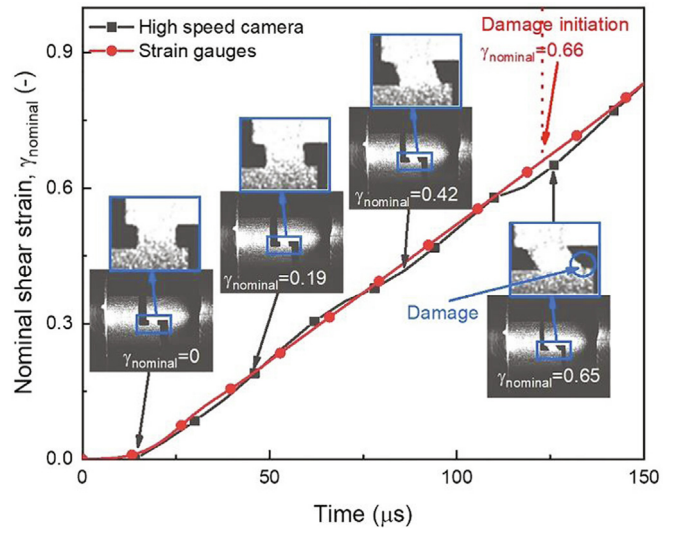


Fig. 6. Comparison of nominal shear strain-time curves between measured by strain gauges on the SHPB bars and measured by a high speed camera.

To check the repeatability of the SSS specimen, three tests were performed under the same conditions. The resulting $\tau_{nominal} - \gamma_{nominal}$ curves are shown in Fig. 7. It is observed that the three curves match each other well, even during the elastic deformation and the damage propagation stage. Therefore, the new shear technique including both the SSS specimen and the SHPB device has good reliability.

The $\tau_{nominal} - \gamma_{nominal}$ curves of 304 ASS under nominal shear strain rates ranging from 3000 s^{-1} to 45000 s^{-1} are shown in Fig. 8. In shear testing at strain rates below 12000 s^{-1} , oscillations due to the Pochhammer-Chree dispersion effect (Chree, 1889; Pochhammer, 1876) are observed. For comparison, the flow stress curves at two quasi-static strain rates 10^{-3} s^{-1} and 10^{-1} s^{-1} are also given in Fig. 8. It is observed from the figure that strain rate has an obvious effect on the shear flow stress curves. The flow stresses are the same for the strain rates 0.001 s^{-1} and 0.1 s^{-1} , but increases continuously with increasing dynamic shear strain rate. Considering the stress oscillation, at nominal shear strain of 0.2, the shear flow stresses are 543 and 573 MPa at 3000 s^{-1} and

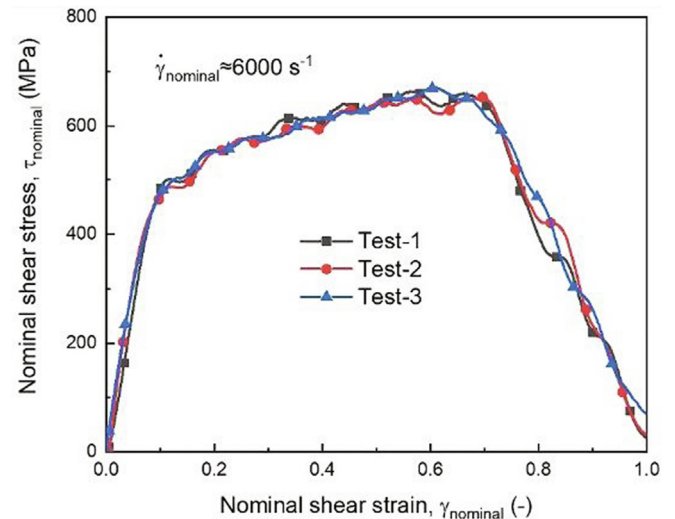


Fig. 7. Nominal shear stress-shear strain curves of three tests conducted under the same conditions.

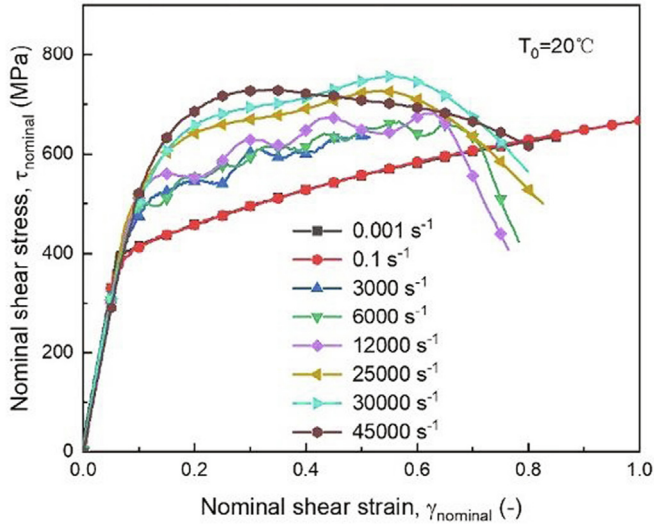


Fig. 8. Nominal shear stress-shear strain curves of 304 ASS at different nominal shear strain rates.

12000 s^{-1} , respectively. Between 12000 s^{-1} to 25000 s^{-1} , an abrupt flow stress increase is observed. This may be caused by strain rate sensitivity of 304 ASS or is due to the different specimen geometry

used for different strain rate regimes. The effect of specimen geometry on the experimentally obtained flow stress curves will be discussed and mitigated by a correction coefficient method introduced in Section 4.3.

The tested SSS specimens with different shear zone width L are shown in Fig. 9. Plastic deformation was confined to the specimen shear zone, while the other elements of the specimen remained elastic. In Fig. 9(a) the shape of the specimen shear zone changed from true rectangular form to a parallelogram, indicating a plane shear deformation mode. In Fig. 9(b) and (c), specimen failure was observed. The cracks propagate along the diagonal of the specimen shear zone, dividing the specimens into two centrally symmetric parts. This phenomenon is often observed in double shear specimens and is attributed to stress concentration at the four corners of the specimen shear zone (Meyer and Halle, 2011; Rusinek and Klepaczko, 2001; Xu et al., 2017).

4. Numerical simulation and discussion

To validate the new shear specimen and the corresponding SHPB technique, numerical simulations of dynamic shear tests have been performed using software ABAQUS/Explicit. A 3D full size finite element (FE) model consisting of the incident bar, the SSS specimen and the transmitted bar was developed, Fig. 10. To reduce the computing time, the projectile is not included in the

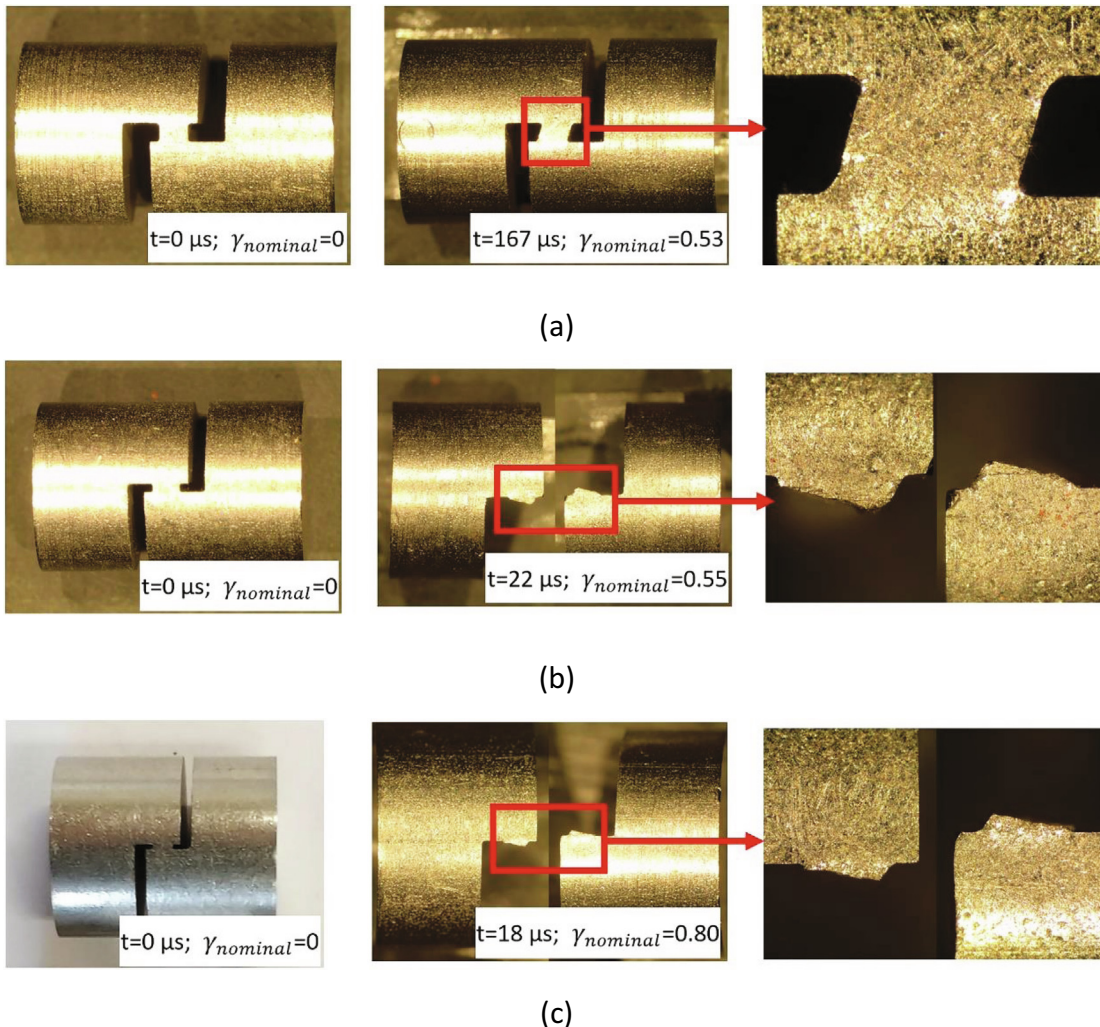


Fig. 9. SSS specimens before and after tests with different shear zone widths L : (a) $L = 1 \text{ mm}$; (b) $L = 0.5 \text{ mm}$; (c) $L = 0.3 \text{ mm}$.

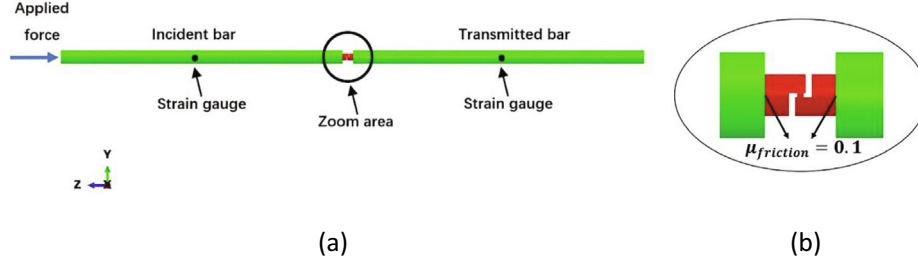


Fig. 10. FE model for numerical simulations: (a) SHPB bars with the SSS specimen, (b) magnification of the SSS specimen.

model. Instead, the experimentally obtained force-time data was applied on the left end face of the incident bar. The frictional contact at the specimen/bar interfaces assume a coefficient of 0.1, a value commonly used for lubricated steels (Dorogoy and Rittel, 2017).

The mesh details of the FE model are shown in Fig. 11. The 8-node linear brick with reduced integration element (C3D8R) is selected for the SHPB bars, while a fully integrated continuum element coupled with temperature element (C3D8T) is selected for the SSS specimen. To reduce calculation time, different mesh sizes were used for various parts of the model. Near the specimen/bar interfaces, a fine mesh of the SHPB bars is used to ensure a good contact between them. The minimum element size is 0.03 mm in the specimen shear zone. The numbers of elements are 156,210 and 139,046 for the SHPB bars and the SSS specimen, respectively.

The material parameters used in the FE model are shown in Table 2. The SHPB bars are defined as elastic. For the SSS specimen, the Johnson-Cook (JC) model derived from the flow stress curves shown in Fig. 8 is used to describe the thermo-viscoplastic behavior. No failure process is taken into consideration.

JC model is a phenomenological model describing the flow stress of materials as a multiplication of several mathematical functions. The model is simple to implement and has a limited number of material parameters. Therefore, it is widely used for various kinds of materials over a wide range of strain rates and temperatures. The model is expressed as:

$$\sigma = (A + B\epsilon_p^n)(1 + C\ln\dot{\epsilon}^*)(1 - T^{*m}) \quad (5)$$

where A , B , n , C and m are material constants, $\dot{\epsilon}^* = \dot{\epsilon}_p/\dot{\epsilon}_{ref}$ is the dimensionless strain rate and $T^* = (T - T_{ref})/(T_m - T_{ref})$ is the

homologous temperature. T , T_m and T_{ref} are the absolute temperature, the melting temperature of 304 ASS and the reference temperature, respectively. The three terms in Eq. (5) describe the strain hardening, strain rate sensitivity and thermal softening effect, respectively. Concerning the identification of model parameters, the method described by Farrokh and Khan (2009) is adopted. The initial values of the JC model are determined following a procedure step by step; then, using a least square method, the five model parameters are implemented to an optimization program to further minimize the difference between experiments and model predictions.

For dynamic shear tests ($\dot{\epsilon}_p \geq 10 \text{ s}^{-1}$), the deformation process is assumed to be adiabatic and the corresponding temperature rise is described by Eq. (6):

$$\Delta T(\dot{\epsilon}) = \frac{\beta}{\rho C_p} \int \sigma d\epsilon_p \quad (6)$$

where β ($=0.9$) is the Taylor-Quinney coefficient characterizing the fraction of plastic work converted into heat, C_p refers to the specific heat of 304 ASS and is assumed as a constant of $500 \text{ J/kg}\cdot^\circ\text{C}$.

According to the $\tau_{nominal} - \gamma_{nominal}$ curves obtained from dynamic shear tests at room temperature, parameters of the JC model are determined and shown in Table 3. Only the dynamic flow stress curves in the range of 3000 s^{-1} to 45000 s^{-1} were fitted to the JC model because the model did not fit the material data across a wider range of strain rates from quasi-static 10^{-3} s^{-1} to high strain rate 45000 s^{-1} . A comparison between the experimental flow stress curves and the predictions by JC model is shown in Fig. 12. The initial elastic deformation of all curves was removed to improve clarity. It is observed the model describes dynamic defor-

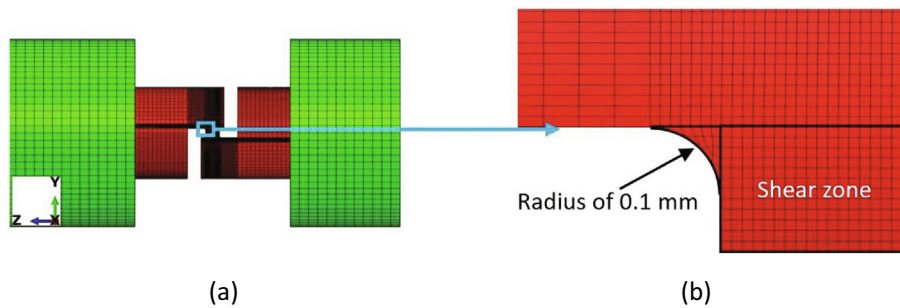


Fig. 11. FE mesh used in the model: (a) bars and the SSS specimen, (b) refined mesh in the shear zone of the SSS specimen.

Table 2
Material parameters used in the numerical simulations.

Part	Material	$\rho(\text{kg/m}^3)$	$E(\text{GPa})$	Poisson's ratio, μ	Thermal conductivity, λ ($\text{W/m}\cdot^\circ\text{C}$)	Specific heat, C_p ($\text{J/kg}\cdot^\circ\text{C}$)
SSS specimen	304 ASS	7.8	210	0.3	16.2	500
SHPB bars	Maraging steel	8.2	210	0.3	(-)	(-)

Table 3
Material constants of the JC model for 304 ASS.

A(MPa)	B(MPa)	n	C	m
657	633	0.609	0.163	1.001

mation behavior of 304 ASS accurately within nominal shear strain rate range between 6000 s^{-1} and 30000 s^{-1} with an average error of 2.78%. The prediction error for the strain rate range 3000 s^{-1} and 45000 s^{-1} is higher (respectively 10.9% and 9.7%). Since the JC model is used for numerical simulation at only dynamic strain rates, the model is supposed to give a good prediction of the material behavior.

4.1. Validity of the strain wave signals in SHPB device

A comparison between the experimental and the numerical strain wave signals at $\dot{\epsilon}_{nominal} = 6000 \text{ s}^{-1}$ is shown in Fig. 13. During numerical simulations, the strain wave signals are measured at exactly the same positions as the strain gauges in experiments. It can be seen from Fig. 13 (a) that within the initial $125 \mu\text{s}$, the incident, reflected and transmitted signals agree well with the experiments. After that, specimen failure occurs in experiments while the failure process is not considered in numerical simulations. Hence, the experimental and numerical signals begin to separate from each other. In general, the numerical simulations can reproduce the experimental shear tests with a certain accuracy. A magnification of the transmitted signals is shown in Fig. 13 (b), indicating an average difference of 4.2% exists between the two curves. Two reasons are possible for this phenomenon: first, the JC model itself cannot describe the deformation behavior of 304 ASS accurately. The model assumes the mechanical properties of materials are multiplicative functions of strain, strain rate and temperature and does not consider the coupling effects. Therefore, researchers have amended the original JC model to enable a more accurate constitutive description of materials (Børvik et al., 2002a, 2002b; Farrokh and Khan, 2009; Khan and Huang, 1992; Khan and Liang, 1999). Second, the $\tau_{nominal} - \gamma_{nominal}$ curves in Fig. 8 may not accurately reflect the shear behavior of 304 ASS. This problem exists in several kinds of shear specimens such as the hat shape specimen or the torsion specimen (Bronkhorst et al., 2006; Peirs et al., 2010; Zhou et al., 2017), and are commonly attributed to the non-uniform stress/strain distribution in the specimen shear zone, and more details on this are presented in Section 4.3.

To obtain a pure shear stress state in the specimen shear zone, the SSS specimen is intentionally not axisymmetric in the shear zone. Deformation of eccentric specimens using the SHPB device (Dorogoy et al., 2015; Fransplass et al., 2015; Zhu et al., 2019) may generate bending waves, which distort the reflected and transmitted signals by superposition of bending waves. This phenomenon is observed in several kinds of non-axisymmetric specimens including the compression specimen under shear-compression loading (Hou et al., 2019a,b), inclined compression specimen for adiabatic shear band characterization (Meyer et al., 1994; Nie et al., 2007) and the shear-compression specimen (Dorogoy et al., 2015; Rittel et al., 2002). It is necessary to investigate the distribution of strain wave signals in the transmitted bar. As shown in Fig. 14, five positions are selected on the cross-section of the transmitted bar. Line AB is parallel to the specimen shear zone and passes through the center point E, while line CD is perpendicular to line AB. The numerical results are shown in Fig. 15. It is observed from Fig. 15(a) at the specimen/bar interface, the distribution of strain wave signals is not uniform. A strong signal is observed at position E while signals at other positions are significantly weaker and remain near zero. With the propagation of the

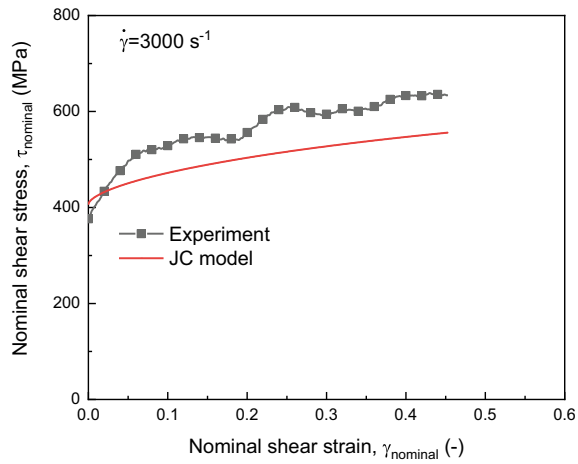
strain waves, the signals at different positions interact and the difference between the five positions decreases continuously. At 0.5 m away from the specimen/bar interface, Fig. 15(b), signals at positions A, B and E become coincident. However, disturbed and complementary signals are observed at positions C and D, with their averages coinciding positions A, B and E. This result demonstrates the influence of bending waves can be eliminated by mounting strain gauges in series. In addition, by extending the length of the transmitted bar from 1.5 m to 3 m in numerical simulations, the signals at five positions along the bar suggest locating the strain gauges at least 1.5 m away from the specimen/bar interface to eliminate bending waves. During dynamic shear tests in this work, the transmitted signals were measured by strain gauges in series at a distance of 0.75 m away from the specimen/bar interface. Therefore, the experimentally-obtained strain wave signals are valid.

The force signal obtained at the specimen/bar interface and the strain gauge positions on the bar is shown in Fig. 16. It is observed the force measurement at the two positions are similar, except the former one has more and irregular oscillations. Hence, during the propagation of strain wave signals along the transmitted bar, the integrated force remains unchanged and represents the actual force acting on the end face of the SSS specimen.

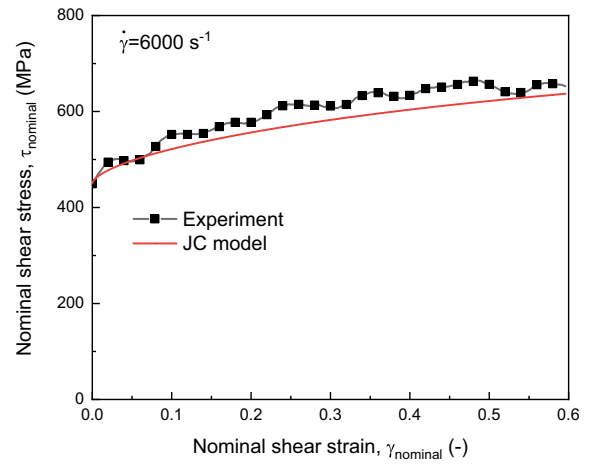
4.2. Analysis of stress state in specimen shear zone

From the numerical results, the stress state in the specimen shear zone is analyzed. The average stress and logarithmic strain components obtained for the specimen shear zone as a function of nominal shear strain are shown in Fig. 17. It is observed during the entire passage of deformation, the specimen is dominated by shear stress component σ_{23} and shear strain component ϵ_{p23} . In Fig. 17 (a), with increasing nominal shear strain, the normal stress components σ_{11} and σ_{33} increase continuously, while the shear stress components σ_{12} and σ_{13} remain at zero. The evolution of stress components in the SSS specimen is similar to that in the double shear specimen (DSS) developed by Xu et al. (2017). Unlike the DSS specimen, the stress component σ_{22} in SSS specimen increases slightly first and declines to zero at large strain. This feature is attributed to specimen being unconstrained and free to move in the lateral direction. Hence, the strong tension component σ_{22} at large strain, which is often observed in classical double shear specimen, is not present in the SSS specimen. In Fig. 17 (b), the evolution of strain components is similar to that of stress components. Shear strain component ϵ_{p23} is always much larger than ϵ_{p22} and ϵ_{p33} , while the other components remain at zero. At a nominal shear strain of 0.66 corresponding to the damage initiation in experiments, the values of ϵ_{p23} , ϵ_{p22} and ϵ_{p33} are -0.38 , -0.07 and 0.07 , respectively. The absolute values of ϵ_{p22} and ϵ_{p33} are 18.4% of ϵ_{p23} . According to the stress/strain components distribution above, deformation of SSS specimen is dominated by shear components σ_{23} and ϵ_{p23} . The other components are comparatively small such that the stress state in specimen shear zone can be regarded as plane shear.

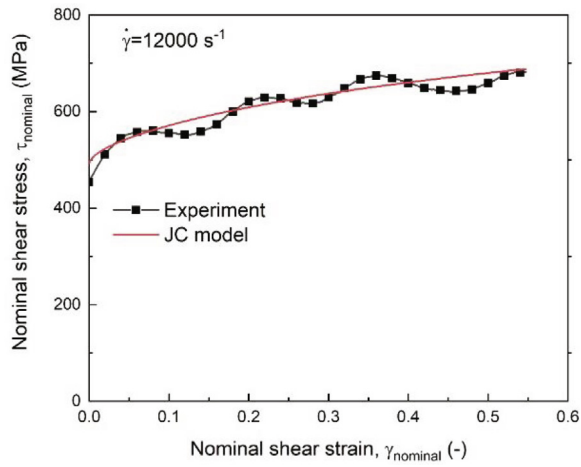
At the damage initiation point ($\gamma_{nominal} = 0.66$), the distribution of Von Mises stress on the central y-z and x-z planes of the specimen shear zone is shown in Fig. 18. It is observed Von Mises stress is uniformly distributed through the specimen shear zone, except the upper and lower areas where a stress gradient varying between 600 MPa and 1300 MPa exists. Away from the shear zone, a strong stress gradient exists. Stress concentration is observed at the four corners of the specimen shear zone. The distribution of equivalent plastic strain at a nominal shear strain of 0.66 is shown in Fig. 19. Plastic deformation is limited to the specimen shear zone and the distribution is uniform. At the upper left and lower right corners of



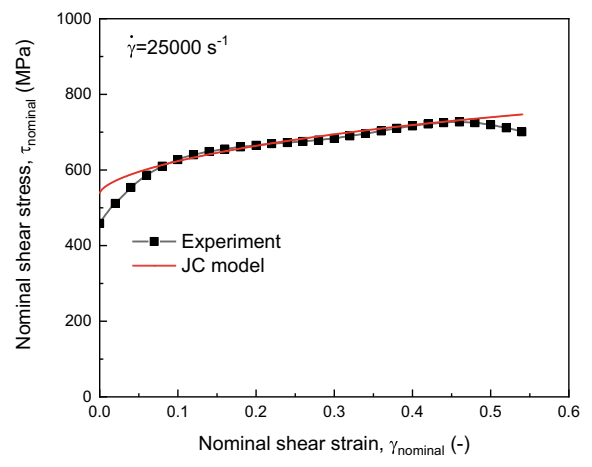
(a)



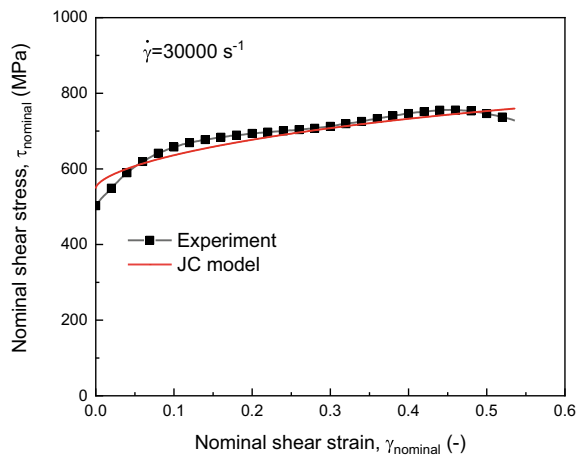
(b)



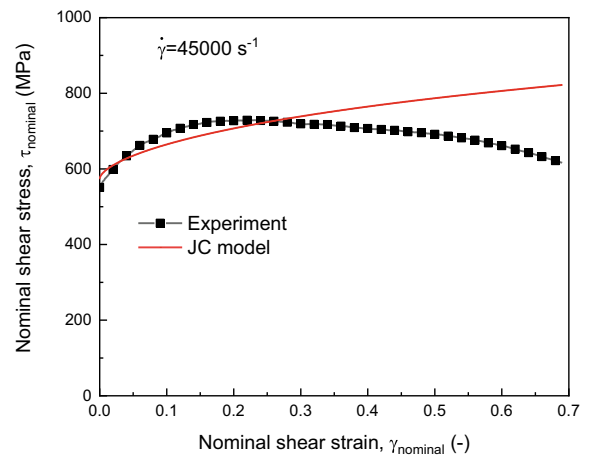
(c)



(d)



(e)



(f)

Fig. 12. Comparison of nominal shear stress-nominal shear strain curves between experiments and JC model at nominal shear strain rates of (a) 3000 s^{-1} , (b) 6000 s^{-1} , (c) 13000 s^{-1} , (d) 25000 s^{-1} , (e) 30000 s^{-1} and (f) 45000 s^{-1} .

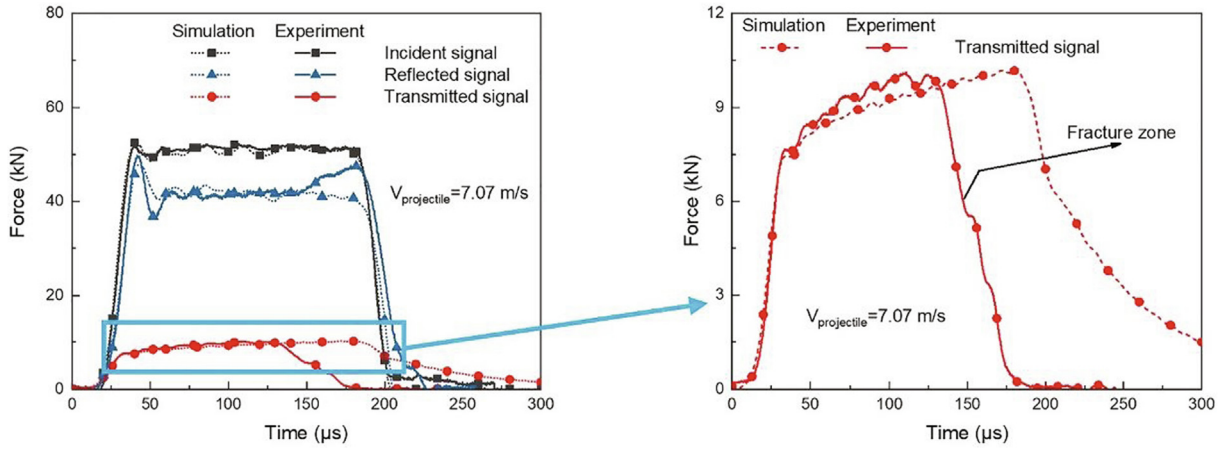


Fig. 13. Comparison of the incident, transmitted and reflected force wave signals between experiments and numerical simulations.

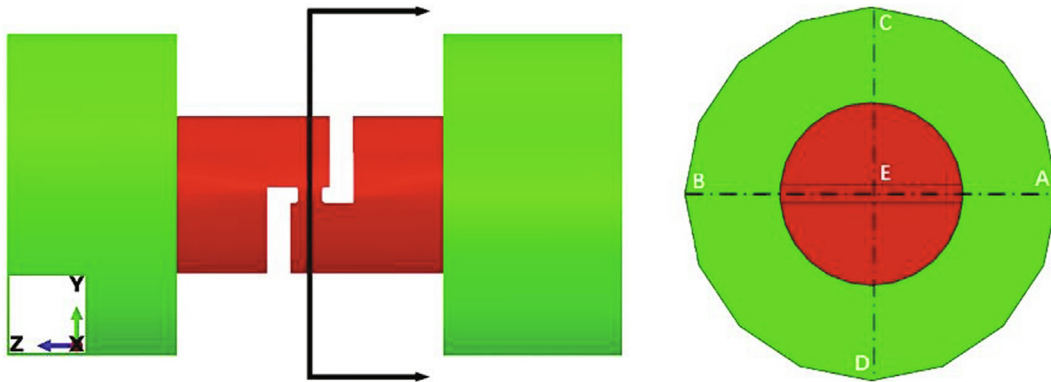


Fig. 14. Schematic diagram of the selected positions on the cross-section of the transmitted bar.

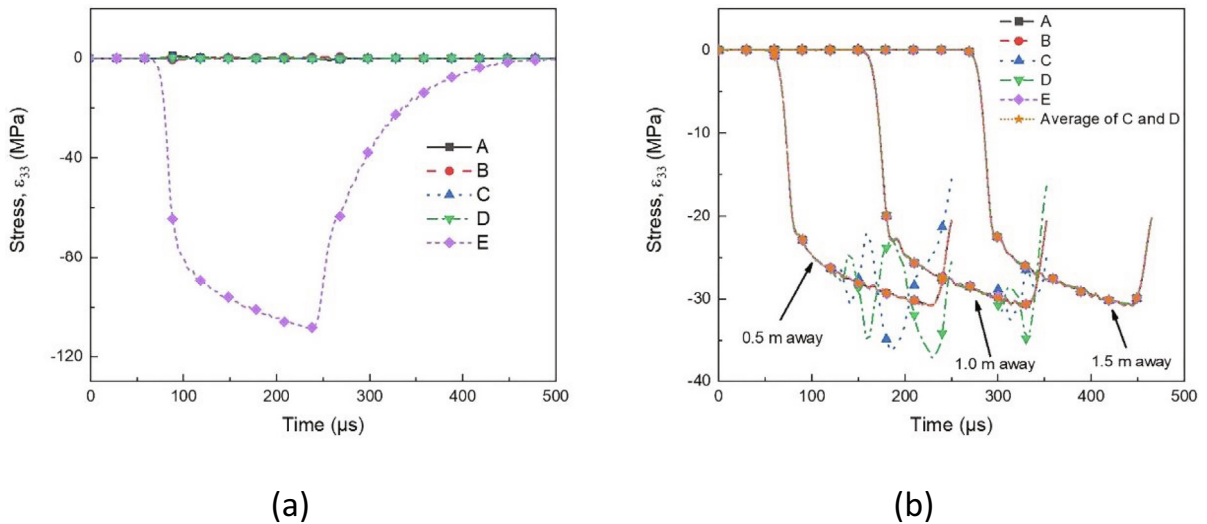


Fig. 15. Transmitted stress wave signals (a) at the bar end and (b) at different locations from the bar end.

the specimen shear zone, the largest plastic strain of 0.61 is observed. It indicates that the specimen may fail along the diagonal direction of the shear zone. This phenomenon verified the fracture patterns shown in Fig. 9.

The evolution of average stress state (η and $\bar{\theta}$) of the entire specimen shear zone with nominal shear strain is calculated and shown

in Fig. 20. During the plastic deformation process, the value of η increases continuously from -0.064 to 0.087 , indicating that the corresponding stress state changes from slight shear-compression to shear-tension. The average η during the whole plastic deformation period is 0.032 . The evolution of $\bar{\theta}$ shows an opposite trend: it decreases quickly from 0.110 at $\epsilon_p = 0$ to 0.007

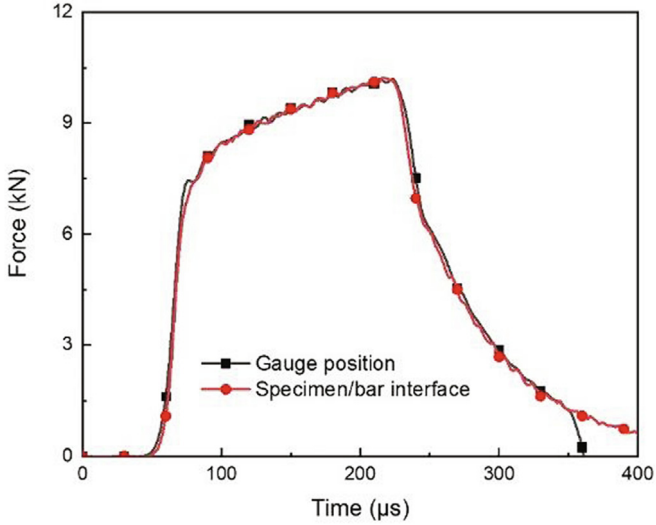


Fig. 16. Comparison of the integrated force at the bar end and from the strain gauges position on the transmitted bar.

at $\varepsilon_p = 0.14$, then declines linearly until the damage initiation point. The average $\bar{\theta}$ over the entire passage of deformation is 0.004. From the analysis of the stress state in the specimen shear zone, values of η and $\bar{\theta}$ are very close to zero, which indicates that stress state in specimen shear zone is simple shear.

Compared to the commonly used double shear specimen (Klepaczko, 1994; Rusinek and Klepaczko, 2001; Shi et al., 2014; Xu et al., 2017), stress state in SSS specimen is relatively closer to pure shear. This is because the SSS specimen is not secured to the bar system, and the end faces of the specimen are coated with a lubricant to reduce friction. During testing, the specimen can move freely in both the longitudinal and the lateral directions. Strong tension components associated with restricted lateral displacement are not present. To verify this finding, another numerical simulation was performed. Boundary conditions of the FE model, Fig. 21, is similar to the double shear specimen with clamping devices shown in Fig. 22. In Fig. 21, a restriction of lateral displacement on two surfaces 0.3 mm away from the specimen shear zone is incorporated in the model. The other boundary conditions

are exactly the same as defined in the FE model in Section 4.1. From the numerical simulations, the average η and $\bar{\theta}$ for the entire region of the specimen shear zone are compared to the results in Fig. 20. From Fig. 23 the effect of the restriction on lateral displacement increases the average η while $\bar{\theta}$ decreases at a faster rate. Compared to the SSS specimen, at the nominal shear strain of 0.66, values of η and $\bar{\theta}$ vary from 0.087 to 0.195 and from -0.023 to -0.066 , an increase of 124% and 187%, respectively. For the FE model with restriction on lateral displacement, the average η and $\bar{\theta}$ of the entire specimen shear zone are 0.081 and -0.027 , respectively. To explain the difference between the results of the two FE models, the thickness reduction of the specimen shear zone with or without lateral displacement restriction is calculated and shown in Fig. 23. It is seen that during deformation, the specimen shear zone reduces in the lateral direction. For SSS specimen, the shear zone thickness decreases from 1 mm to 0.959 mm, a thickness reduction of 0.041 mm. While for SSS specimen with lateral displacement restriction, the thickness reduction is significantly smaller, merely 0.012 mm. Hence, the tension components along the lateral direction become obvious at large deformation, and the corresponding stress state deviates from pure shear.

The stress state along 10 paths in the specimen shear zone is analyzed. As shown in Fig. 24, paths A1-A5 are identified on the central X-Z plane, while paths B1-B5 are on the central Y-Z plane. The five paths divide the specimen shear zone equally into 6 sections.

The distribution of η and $\bar{\theta}$ on the central X-Z plane at a nominal shear strain of 0.66 is shown in Fig. 25. It is observed from Fig. 25 (a) that η is always positive along the five paths with exception to a few fluctuation points, indicating a slight shear-tension stress state in the specimen shear zone. Evolution of η along paths A2-A4 are similar. At the left and right free surfaces of the specimen shear zone a slight fluctuation is observed; at positions between 1.79 mm and 8.21 mm, η is uniformly distributed between 0.012 and 0.036, with an average value of 0.030. For paths A1 and A5, they are close to the upper and lower surfaces of the specimen shear zone. Due to the non-uniform distribution of the stress/strain components, values of η fluctuate significantly between -0.047 and 0.141. The distribution of $\bar{\theta}$ along the five paths is shown in Fig. 25 (b). From 1.40 mm to 8.60 mm, they are all similar, and the values decrease monotonically first and then increases continuously, obtaining a minimum of 0.002 at the center position. For

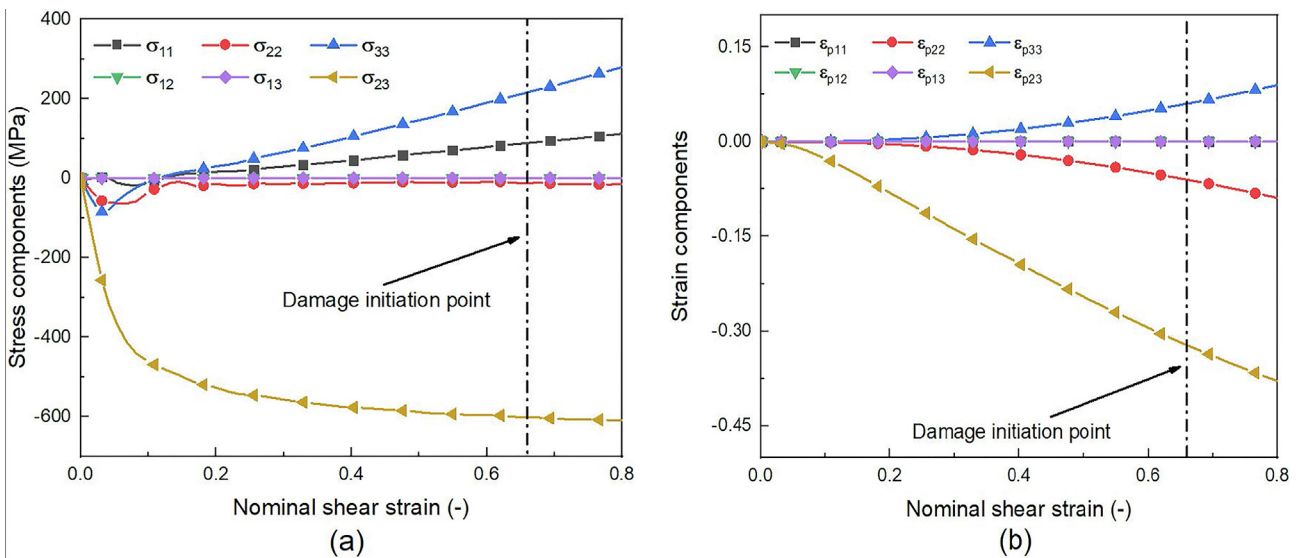


Fig. 17. Average values of stress and strain components in the whole shear zone. (a) Stress components and (b) strain components.

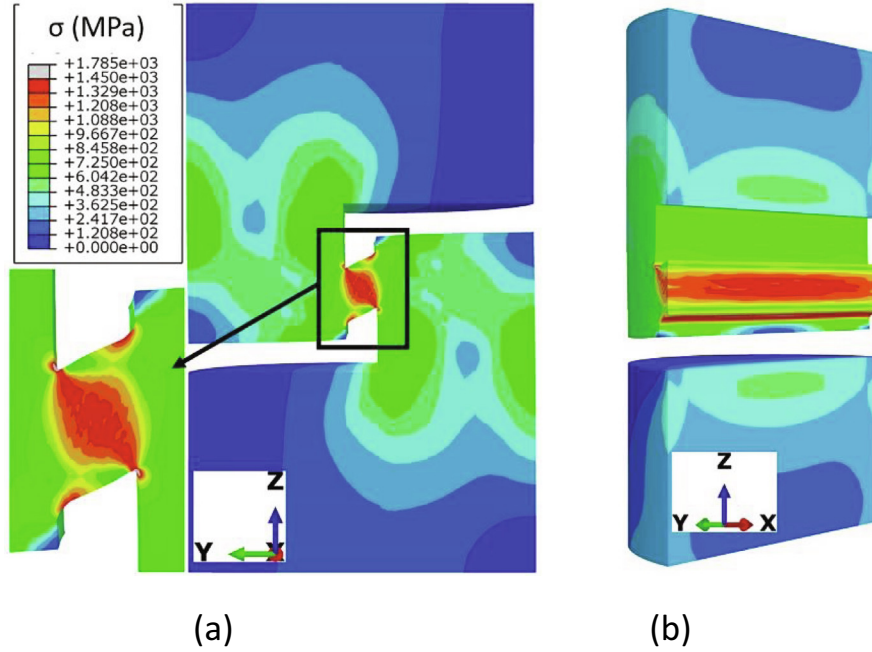


Fig. 18. Distribution of Von Mises stress on the central (a) y-z plane and (b) x-z plane of the shear zone at a nominal shear strain of 0.66.

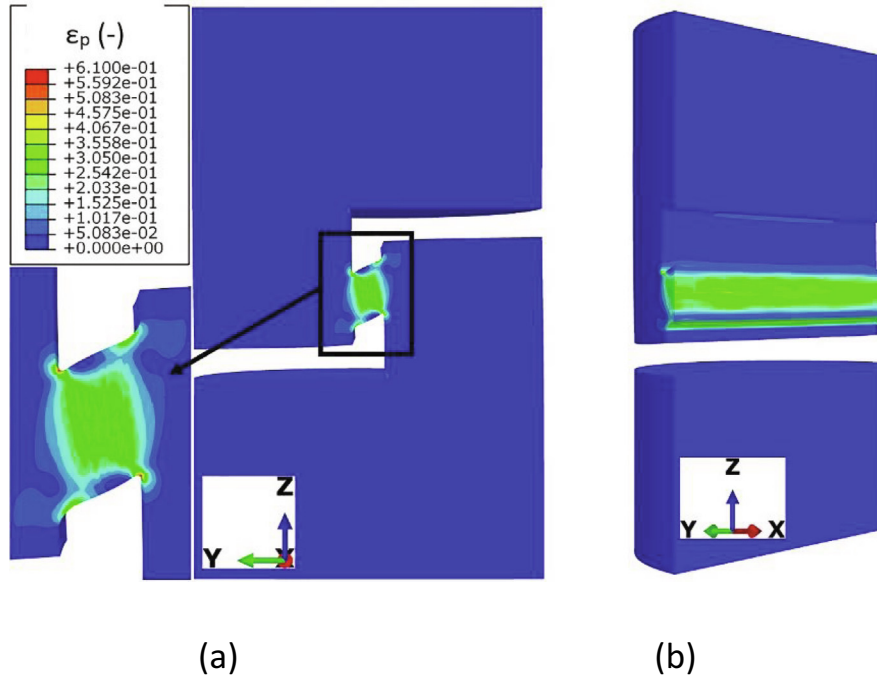


Fig. 19. Distribution of equivalent plastic strain on the central (a) y-z plane and (b) x-z plane of the shear zone at a nominal shear strain of 0.66.

positions close to the left and right free surfaces, values of $\bar{\theta}$ become negative in the range between -0.18 and -0.06 . Values of $\bar{\theta}$ along paths A1 and A5 are comparatively smaller than along paths A2 to A4.

The distribution of η and $\bar{\theta}$ on the central Y-Z plane at a nominal shear strain of 0.66 is shown in Fig. 26. To reach strain rates above 10^4 s^{-1} , the specimen width is designed to be 1 mm. Hence, distribution of η along paths B1-B5 is not as uniform as along paths A1-A5. It is observed from Fig. 26 (a) on the left edge of the specimen

shear zone, values of η increase continuously from -0.377 at B1 to 0.653 at B5, while the situation reversed at the right edge. It indicates that at the left edge of the specimen shear zone, the stress state changes from shear-compression at B1 to shear-tension at B5. This is because the specimen is designed as a single shear zone which is not axis-symmetric to the circular cross-section of the test bar system. During testing, the shear zone has a tendency to rotate, so that the material at position B1 is in compression and changes gradually into tension at position B5. The small radii on the upper

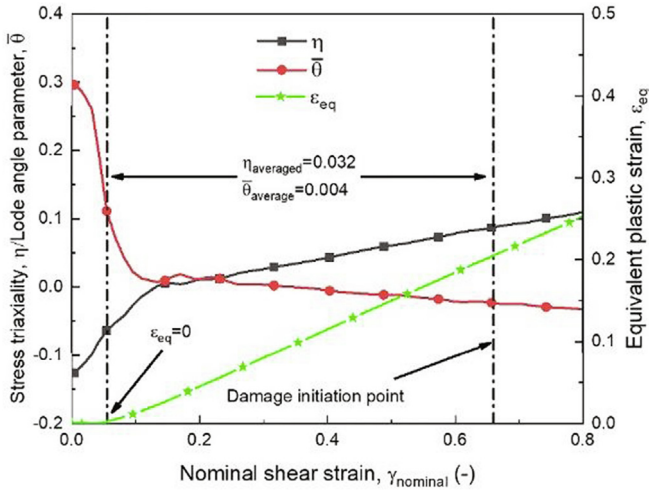


Fig. 20. Evolution of average stress triaxiality η , Lode angle parameter $\bar{\theta}$ and equivalent plastic strain ϵ_{eq} of the whole shear zone with nominal shear strain.

and lower surfaces of the specimen shear zone influence the evolution of η along paths B1 and B5 and this is more obvious than that along paths B2 to B4. It is observed from Fig. 26 (b) that the distribution of $\bar{\theta}$ along the five paths is different from that of η . Along paths B2 to B4, $\bar{\theta}$ changes little and basically fluctuates between -0.006 and 0.009 . For path B1, the value of $\bar{\theta}$ increases in the left half width and then remains constant in the right half width; while for path B5, an opposite trend is observed. Along all five paths, the average value of $\bar{\theta}$ is 0.00058 , which is close to zero.

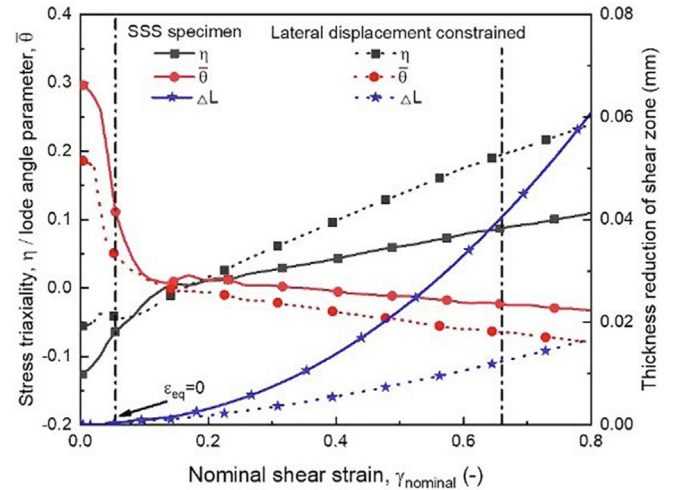


Fig. 23. Evolution of average stress triaxiality η and Lode angle parameter $\bar{\theta}$ as well as the thickness reduction of the shear zone with nominal shear strain.

4.3. Determination of stress-strain relation using the SSS specimen

One of the aims of designing SSS specimen is to obtain accurate shear stress-shear strain relations for constitutive behavior modeling. Hence, in this section, the correct shear stress-shear strain behavior of 304 is derived from the measurement of force and displacement and then verified by numerical simulations.

From the numerical results in Section 4.1, a comparison between the average stress-strain relation of all elements in the

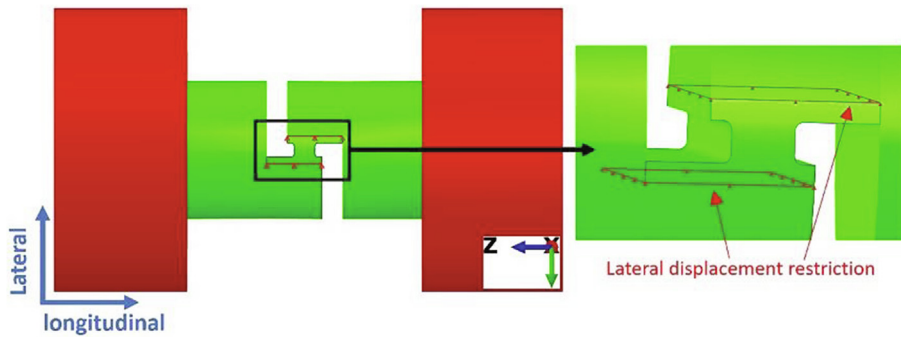


Fig. 21. Additional boundary conditions of the second FE model.

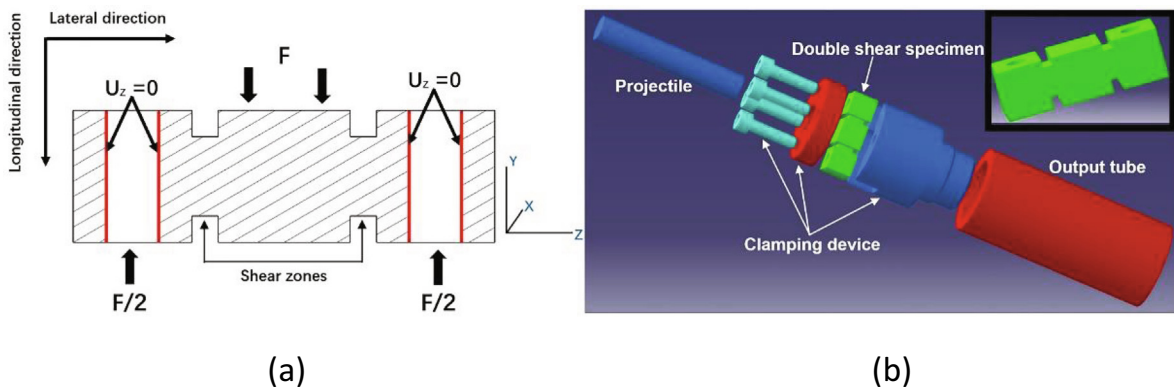


Fig. 22. Double shear specimen for direct impact technique. (a) Boundary conditions of the specimen, (b) assembly of the specimen, clamping system and direct impact device (Klepaczko, 1994).

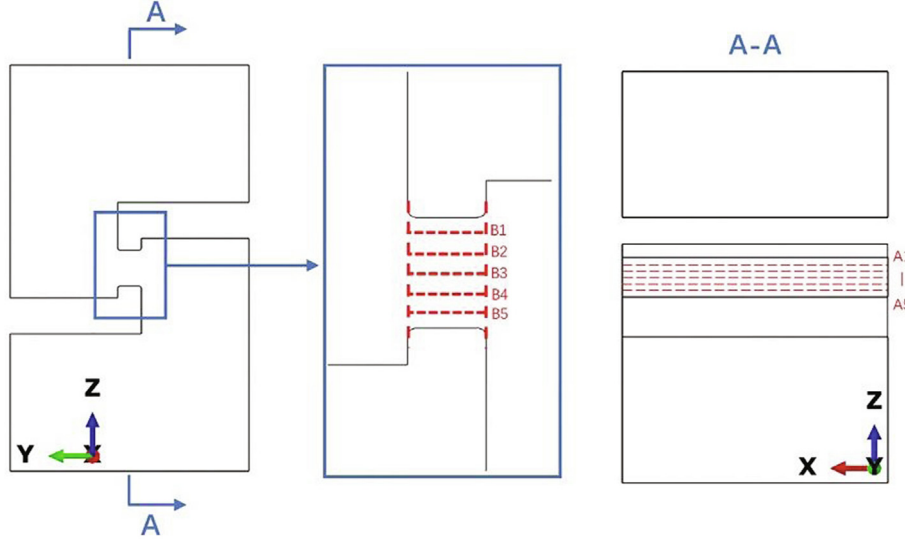


Fig. 24. Selected paths in the shear zone for stress state analysis. Paths A1-A5 are on the central x-z plane of the shear zone and Paths B1-B5 are on the central y-z plane of the shear zone.

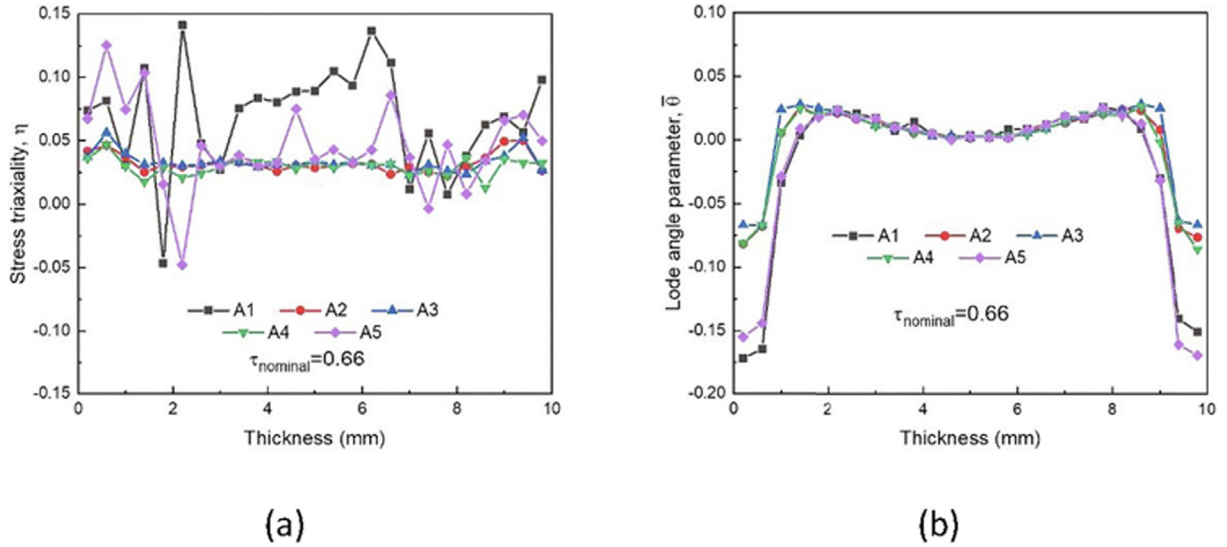


Fig. 25. Distribution of (a) stress triaxiality η and (b) Lode angle parameter $\bar{\theta}$ along paths A1-A5 in the shear zone at nominal shear strain of 0.66.

specimen shear zone (representing the input model to Abaqus) and the $\tau_{nominal} - \gamma_{nominal}$ curve calculated from the force-displacement results (representing the macroscopic response of the entire specimen) is shown in Fig. 27. For brevity of comparison, the $\tau_{nominal} - \gamma_{nominal}$ curve is converted to the Von Mises stress-equivalent plastic strain ($\sigma_{eq} - \varepsilon_{eq}$) curve by the following equations.

$$\sigma_{eq} = \sqrt{3}\tau_{nominal} \quad (7)$$

$$\varepsilon_{eq} = \frac{\gamma_{nominal}}{\sqrt{3}} \quad (8)$$

It is observed that a difference exists between the two curves. The calculated curve underestimates the correct flow stress with an average error of 11%. This is mainly because a pure shear stress state is assumed when converting the $\tau_{nominal} - \gamma_{nominal}$ curve into the $\sigma_{eq} - \varepsilon_{eq}$ curve, while the actual stress state in the specimen shear zone deviates slightly from pure shear. At the initial stage of deformation, a significant difference is observed between the

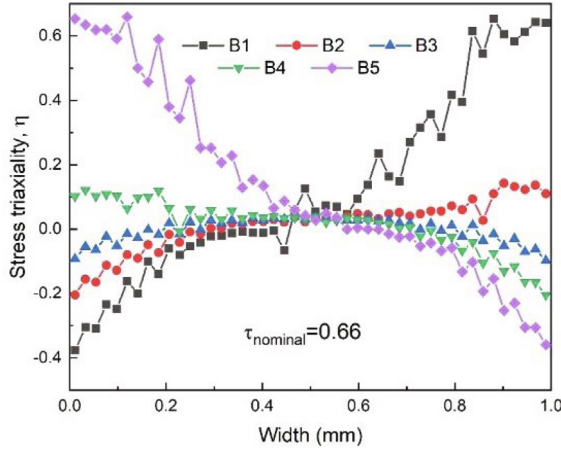
two curves. A similar phenomenon was observed by Rittel et al. (2002) in SCS specimens and by Shi et al. (2014) in double shear specimens, and is reported to be caused by stiffness exaggeration of areas outside the specimen shear zone. From the preceding analysis, the experimentally obtained $\tau_{nominal} - \gamma_{nominal}$ curves cannot represent the correct shear behavior of 304 ASS. Hence, a correction to the experimental data is necessary to accurately characterize shear stress-shear strain behavior.

In this work, a correction coefficient method proposed by Campbell and Ferguson (1970) is applied to derive the correct shear stress-shear strain ($\tau - \gamma$) curves from the nominal shear stress-nominal shear strain ($\tau_{nominal} - \gamma_{nominal}$) results.

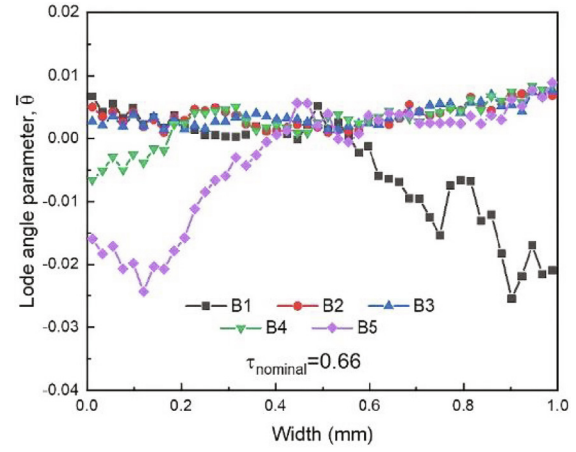
$$\gamma = \bar{\lambda}_{\gamma}(\gamma_{nominal} - \gamma_{yield}) \quad (9)$$

$$\tau = \bar{\lambda}_{\tau}\tau_{nominal} \quad (10)$$

where $\bar{\lambda}_{\gamma}$ and $\bar{\lambda}_{\tau}$ are the average correction coefficients for shear strain and shear stress, respectively. γ_{yield} is the nominal shear strain



(a)



(b)

Fig. 26. Distribution of (a) stress triaxiality η and (b) Lode angle parameter $\bar{\theta}$ along paths B1-B5 in the shear zone at a nominal shear strain of 0.66.

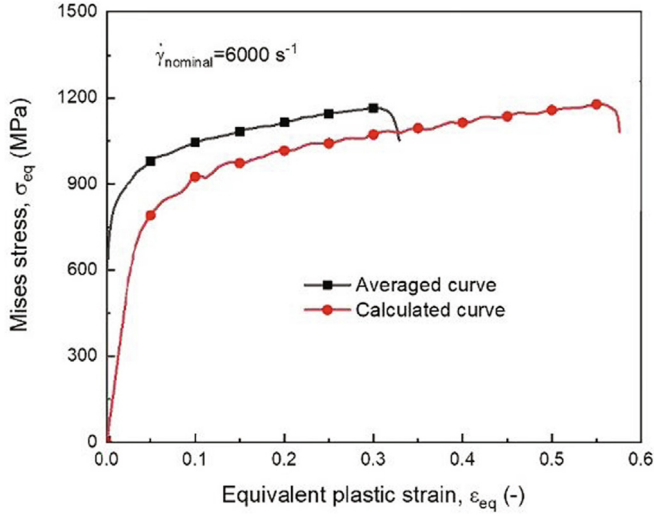


Fig. 27. Comparison between the average stress-strain curve of all elements in the shear zone and the curve calculated according to force-displacement data.

at which the specimen begins to yield. By comparing the $\tau_{nominal} - \gamma_{nominal}$ curve with the average $\tau - \gamma$ data of all elements in the specimen shear zone, values of $\bar{\lambda}_\gamma$ and $\bar{\lambda}_\tau$ can be determined. A detailed description of the procedure can be found in Appendix A. The correction coefficients for SSS specimens with different shear zone width L are shown in Table 4.

With the correction coefficient method introduced above, the $\tau_{nominal} - \gamma_{nominal}$ curves in Fig. 8 are converted into the actual $\tau - \gamma$ curves shown in Fig. 28 (a). The effects of shear strain rate on the flow stress and the average strain hardening rate are also calculated and shown in Fig. 28 (b). It is seen from the two figures that the strain rate has a significant effect on the flow stress. The stress remains constant in the quasi-static regime and then increases abruptly under dynamic strain rates. For example, at the nominal shear strain of 0.1, the flow stresses at strain rates 0.001 s^{-1} and 0.1 s^{-1} are 492 and 502 MPa. In the range of 3360 s^{-1} to 26100 s^{-1} , the flow stress increases abruptly from 594 to 722 MPa with an increase of 21.5%. The strong strain rate sensitivity at higher strain rates is observed in many metallic

Table 4

Correction coefficients for SSS specimens with different shear zone width L .

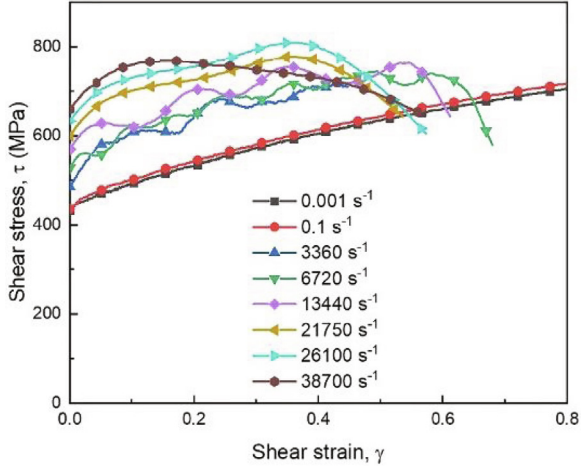
Specimen shear zone width L (mm)	$\bar{\lambda}_\gamma$	$\bar{\lambda}_\tau$
0.3	1.055	0.860
0.5	1.070	0.870
1.0	1.030	1.120

materials and is commonly attributed to the viscous drag effect (Armstrong and Zerilli, 1988) or the enhanced dislocation accumulation rate (Zerilli and Armstrong, 1992). The strain hardening rate is also affected by the shear strain rate. In the range of 0.001 s^{-1} and 0.1 s^{-1} , the average strain hardening rates are around 400 MPa/unit strain; in the range of 3360 s^{-1} to 26100 s^{-1} , the strain hardening rate decreases monotonically from 400 to 310 MPa/unit strain. At the maximum shear strain rate of 38700 s^{-1} , a negative strain hardening rate due to the strong adiabatic heating effect is observed. The material flow stress increases quickly to a peak value and then decreases monotonically.

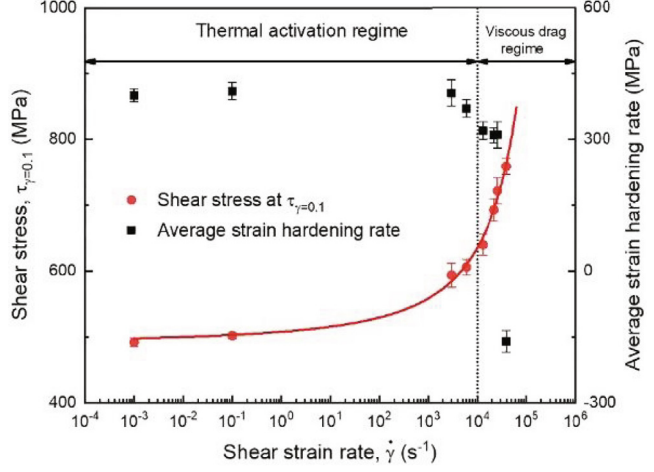
5. Conclusion

In this work, a new SSS specimen has been developed to study shear behavior of bulk metals over a wide range of shear strain rates (within 10^5 s^{-1}) using the conventional SHPB device. This specimen was shown to have several advantages. The geometry is designed to be simple and is easy to manufacture by conventional machining. No clamping system is needed to secure the specimen to the SHPB bars so that it can be tested conveniently under a simple shear stress state. The dimensions of the specimen shear zone can vary in the range of 0.3 to 1.0 mm, so the deformation behavior of materials under extremely high strain rates exceeding 10^4 s^{-1} can be investigated easily.

With the SSS specimen and the SHPB device, shear behavior of 304 ASS over a wide range of shear strain rates between 0.001 s^{-1} and 38700 s^{-1} at room temperature has been studied. From the experimental results and numerical simulations, the shear testing technique was shown to be reproducible, and force equilibrium state within the specimen and reliability of strain wave signals are verified. During testing, the specimen shear zone is dominated by simple shear with low stress triaxiality and Lode angle param-



(a)



(b)

Fig. 28. (a) Corrected shear stress-shear strain curves of 304 ASS at different shear strain rates. (b) Evolution of shear stress and average strain hardening rate with shear strain rate.

eter. In addition, a correction coefficient method is used to derive the correct shear stress-shear strain behavior of the material from the measured force-displacement results. From the corrected shear stress-shear strain curves, the strain rate is observed to have a significant effect on deformation behavior of 304 ASS. Under dynamic shear strain rates, the flow stress increases abruptly with increasing strain rate, while the corresponding strain hardening rate declines monotonically. At the highest shear strain rate of 38700 s^{-1} , a negative strain hardening rate is observed.

Declaration of Competing Interest

The authors declare that they have no known competing financial interests or personal relationships that could have appeared to influence the work reported in this paper.

Acknowledgement

Part of this work was financially supported by the China Scholarship Council (CSC) under Grant 201606220056.

Appendix A. Correction of shear stress-shear strain relations for SSS specimen

Numerical simulation of a quasi-static shear test using the SSS specimen has been conducted by Abaqus/Standard. It aims to determine the relationship between the nominal shear stress-nominal shear strain ($\tau_{nominal} - \gamma_{nominal}$) and the average shear stress-shear strain ($\tau - \gamma$) of all elements in the specimen shear zone using the following equations:

$$\gamma = \bar{\lambda}_\gamma (\gamma_{nominal} - \gamma_{yield}) \quad (A1)$$

$$\tau = \bar{\lambda}_\tau \tau_{nominal} \quad (A2)$$

where γ_{yield} refers to the nominal shear strain at which the SSS specimen begins to yield.

The boundary conditions of the FE model are shown in Fig. A1a. The model consists of a SSS specimen and a rigid plate locates on the upper surface of the specimen. A vertical downward displace-

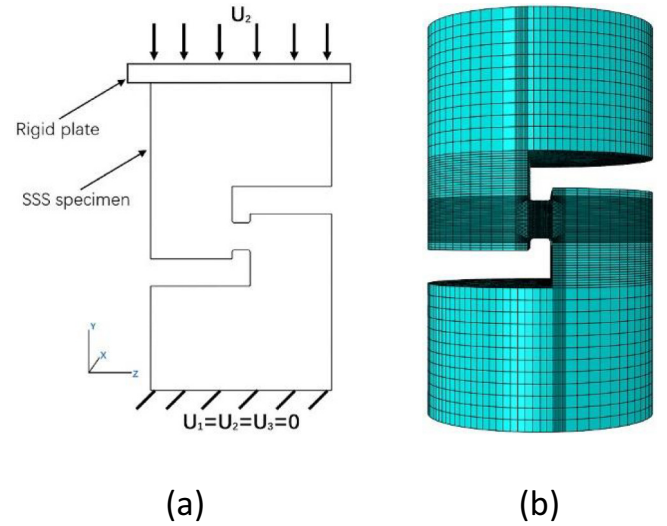


Fig. A1. (a) Boundary conditions of the FE model. (b) Mesh details of the SSS specimen.

ment of 1 mm, corresponding to a nominal shear strain of 1.0, is applied on the rigid plate while the bottom surface of the specimen is fixed. Frictional contact between the rigid plate and the specimens is assumed with a coefficient of 0.1. The mesh details of the model are shown in Fig. A1b. It consists of 118,130 elements C3D8R with a minimum size of 0.03 mm in the specimen shear zone.

An elastic-plastic constitutive model, as shown in Fig. A2, is used in the numerical simulations. The curve is derived from dynamic compression tests of 304 ASS under strain rate of 2500 s^{-1} at room temperature. The Young's modulus is $E = 210 \text{ GPa}$ and Poisson's ratio $\nu = 0.33$. The yield stress σ_0 was taken as 1050 MPa and the strain hardening behavior is described by the Voce type law (1948) $\sigma = \sigma_0 + A(1 - e^{-C\epsilon_{sp}})$ with values of A and C being 888 and 3.14, respectively.

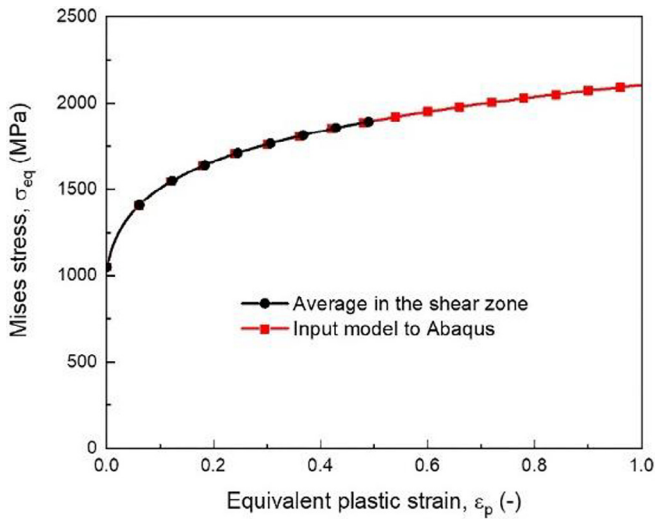
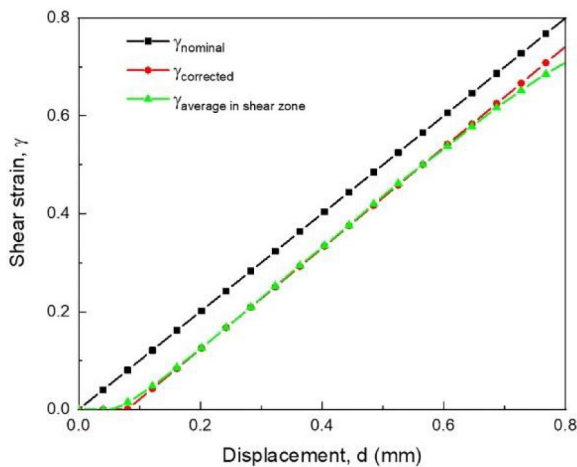


Fig. A2. Average Von Mises stress–equivalent plastic strain curve of the whole shear zone and the flow stress curve input to Abaqus.

According to the numerical results, the average Von Mises stress versus the equivalent plastic strain of all elements in the specimen shear zone is also plotted in Fig. A2. It is seen that the average values represent the constitutive behavior of the simulated material correctly.

Fig. A3 shows the average shear strain in the specimen shear zone and the nominal shear strain versus the applied displacement. From the ratio between the two curves, the correction parameter $\bar{\lambda}_\gamma$ is determined to be 1.03. Fig. A3b shows the evolution of the average shear stress in the specimen shear zone and the nominal shear stress with the applied displacement. Using a least square method, the value of $\bar{\lambda}_\tau$ is fitted to be 1.12. For SSS specimens with shear zone width of 0.5 mm and 0.3 mm, the data correction procedures are exactly the same.

A comparison of the stress–strain curves from the nominal, the corrected and the average value in the specimen shear zone is



(a)

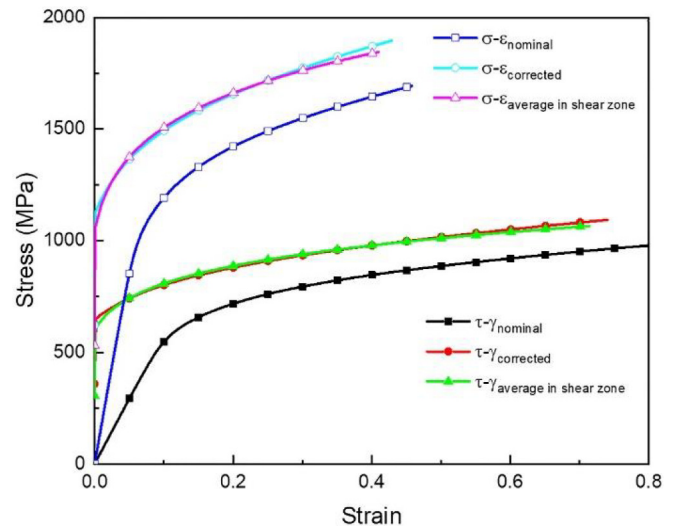
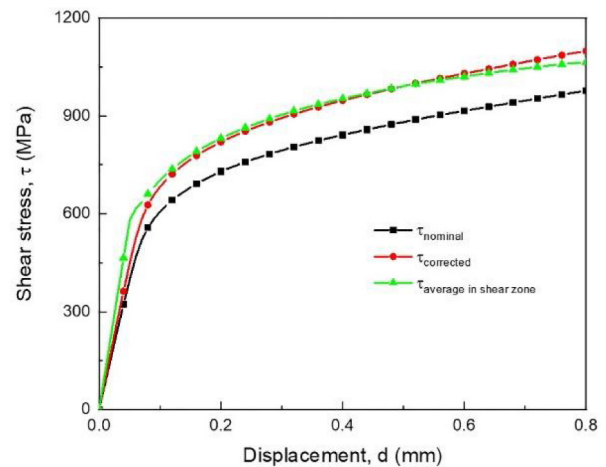


Fig. A4. Comparison between the nominal stress–strain curve, the corrected curve and the average value of the whole shear zone considering both shear stress–shear strain type and Von Mises stress–equivalent plastic strain type evolution.

shown in Fig. A4. It is seen that the correction of the nominal data by the three coefficients $\bar{\lambda}_\gamma$, $\bar{\lambda}_\tau$ and y_{yield} leads to an increase of shear stress and a decrease of shear strain. After correction, the flow stress curve matches the real deformation behavior of the tested material well. In fact, the relative errors for shear stress and shear strain data are 1.0% and 0.9%, respectively. Therefore, Eq. A. 1 and Eq. A. 2 can be used to determine the shear stress–shear strain relations of the tested materials accurately.

Appendix B. Supplementary data

Supplementary data to this article can be found online at <https://doi.org/10.1016/j.ijsolstr.2020.08.019>.



(b)

Fig. A3. (a) Comparison between the nominal shear strain according to applied displacement, the corrected curve and the average shear strain of the whole shear zone. (b) Comparison between the nominal shear stress according to the applied force, the corrected curve and the average shear stress of the whole shear zone.

References

- Arias, A., Rodríguez-Martínez, J.A., Rusinek, A., 2008. Numerical simulations of impact behaviour of thin steel plates subjected to cylindrical, conical and hemispherical non-deformable projectiles. *Eng. Fract. Mech.* 75, 1635–1656. <https://doi.org/10.1016/j.engfracmech.2007.06.005>.
- Armstrong, R.W., Zerilli, F.J., 1988. DISLOCATION MECHANICS BASED ANALYSIS OF MATERIAL DYNAMICS BEHAVIOR. *J. Phys. Colloques* 49, C3-529-C3-534. <https://doi.org/10.1051/jphyscol:1988374>.
- Bai, Y., Wierzbicki, T., 2008. A new model of metal plasticity and fracture with pressure and Lode dependence. *Int. J. Plast.* 24, 1071–1096. <https://doi.org/10.1016/j.ijplas.2007.09.004>.
- Bao, Y., Wierzbicki, T., 2004. On fracture locus in the equivalent strain and stress triaxiality space. *Int. J. Mech. Sci.* 46, 81–98. <https://doi.org/10.1016/j.ijmecsci.2004.02.006>.
- Bonnet-Lebouvier, A.S., Klepaczko, J.R., 2002. Numerical study of shear deformation in Ti-6Al-4V at medium and high strain rates, critical impact velocity in shear. *Int. J. Impact Eng.* 27, 755–769. [https://doi.org/10.1016/S0734-743X\(02\)00010-6](https://doi.org/10.1016/S0734-743X(02)00010-6).
- Børvik, T., Hopperstad, O.S., Berstad, T., Langseth, M., 2002a. Perforation of 12mm thick steel plates by 20mm diameter projectiles with flat, hemispherical and conical noses: Part II: numerical simulations. *Int. J. Impact Eng.* 27, 37–64. [https://doi.org/10.1016/S0734-743X\(01\)00035-5](https://doi.org/10.1016/S0734-743X(01)00035-5).
- Børvik, T., Langseth, M., Hopperstad, O.S., Malo, K.A., 2002b. Perforation of 12mm thick steel plates by 20mm diameter projectiles with flat, hemispherical and conical noses: Part I: experimental study. *Int. J. Impact Eng.* 27, 19–35. [https://doi.org/10.1016/S0734-743X\(01\)00034-3](https://doi.org/10.1016/S0734-743X(01)00034-3).
- Bronkhorst, C.A., Cerrera, E.K., Xue, Q., Maudlin, P.J., Mason, T.A., Gray, G.T., 2006. An experimental and numerical study of the localization behavior of tantalum and stainless steel. *Int. J. Plast.* 22, 1304–1335. <https://doi.org/10.1016/j.ijplas.2005.10.002>.
- Campbell, J.D., Ferguson, W.G., 1970. The temperature and strain-rate dependence of the shear strength of mild steel. *Philos. Mag. J. Theor. Experim. Appl. Phys.* 21, 63–82. <https://doi.org/10.1080/14786437008238397>.
- Chen, Y., Clausen, A.H., Hopperstad, O.S., Langseth, M., 2009. Stress-strain behaviour of aluminium alloys at a wide range of strain rates. *Int. J. Solids Struct.* 46, 3825–3835. <https://doi.org/10.1016/j.ijsolstr.2009.07.013>.
- Chree, C., 1889. The equations of an isotropic elastic solid in polar and cylindrical co-ordinates their solution and application. *Trans. Cambridge Philos. Soc.* 14, 250.
- Dorogoy, A., Rittel, D., 2017. Dynamic large strain characterization of tantalum using shear-compression and shear-tension testing. *Mech. Mater.* 112, 143–153. <https://doi.org/10.1016/j.mechmat.2017.06.003>.
- Dorogoy, A., Rittel, D., Godinger, A., 2016. A shear-tension specimen for large strain testing. *Exp. Mech.* 56, 437–449. <https://doi.org/10.1007/s11340-015-0106-1>.
- Dorogoy, A., Rittel, D., Godinger, A., 2015. Modification of the shear-compression specimen for large strain testing. *Exp. Mech.* 55, 1627–1639. <https://doi.org/10.1007/s11340-015-0057-6>.
- Duan, Q., Jin, T., Chen, S., Shu, X., 2017. Mechanical analysis of PA66 under combined shear-compression. *Appl. Phys. A* 123, 365. <https://doi.org/10.1007/s00339-017-0988-0>.
- Duffy, J., Campbell, J.D., Hawley, R.H., 1971. On the use of a torsional split hopkinson bar to study rate effects in 1100-0 aluminum. *J. Appl. Mech.* 38, 83–91. <https://doi.org/10.1115/1.3408771>.
- Dunand, M., Mohr, D., 2017. Predicting the rate-dependent loading paths to fracture in advanced high strength steels using an extended mechanical threshold model. *International Journal of Impact Engineering*, In Honour of the Editor-in-Chief, Professor Magnus Langseth, on his 65th Birthday 108, 272–285. <https://doi.org/10.1016/j.ijimpeng.2017.02.020>.
- Farrokh, B., Khan, A.S., 2009. Grain size, strain rate, and temperature dependence of flow stress in ultra-fine grained and nanocrystalline Cu and Al: synthesis, experiment, and constitutive modeling. *Int. J. Plast.* 25, 715–732. <https://doi.org/10.1016/j.ijplas.2008.08.001>.
- Francart, C., Demarty, Y., Bahlouli, N., Ahzi, S., 2017. Dynamic Characterization and Modeling of Ductile Failure of Sintered Aluminum Alloy through Shear-compression Tests. *Procedia Engineering*, DYMAT 23rd Technical Meeting - International Conference on Dynamic Fracture of Ductile Materials 197, 69–78. <https://doi.org/10.1016/j.proeng.2017.08.083>.
- Fransplass, H., Langseth, M., Hopperstad, O.S., 2015. Experimental and numerical study of threaded steel fasteners under combined tension and shear at elevated loading rates. *Int. J. Impact Eng.* 76, 118–125. <https://doi.org/10.1016/j.ijimpeng.2014.08.004>.
- Fras, T., Roth, C.C., Mohr, D., 2018. Fracture of high-strength armor steel under impact loading. *Int. J. Impact Eng.* 111, 147–164. <https://doi.org/10.1016/j.ijimpeng.2017.09.009>.
- Gray, G.T., Vecchio, K.S., Livescu, V., 2016. Compact forced simple-shear sample for studying shear localization in materials. *Acta Mater.* 103, 12–22. <https://doi.org/10.1016/j.actamat.2015.09.051>.
- Grytten, F., Børvik, T., Hopperstad, O.S., Langseth, M., 2009. Low velocity perforation of AA5083-H116 aluminium plates. *Int. J. Impact Eng.* 36, 597–610. <https://doi.org/10.1016/j.ijimpeng.2008.09.002>.
- Guo, Y., Li, Y., 2012. A novel approach to testing the dynamic shear response of Ti-6Al-4V. *Acta Mech. Solida Sin.* 25, 299–311. [https://doi.org/10.1016/S0894-9166\(12\)60027-5](https://doi.org/10.1016/S0894-9166(12)60027-5).
- Harding, J., Huddart, J., 1980. The use of the double-notch shear test in determining the mechanical properties of uranium at very high rates of strain. *Mechanical properties at high rates of strain*, 1979.
- Hou, B., Wang, Y., Sun, T.F., Liu, J.G., Zhao, H., 2019a. On the quasi-static and impact responses of aluminum honeycomb under combined shear-compression. *Int. J. Impact Eng.* 131, 190–199. <https://doi.org/10.1016/j.ijimpeng.2019.05.005>.
- Hou, B., Xiao, R., Sun, T.F., Wang, Y., Liu, J.G., Zhao, H., Li, Y.L., 2019b. A new testing method for the dynamic response of soft cellular materials under combined shear-compression. *Int. J. Mech. Sci.* 159, 306–314. <https://doi.org/10.1016/j.ijmecsci.2019.05.039>.
- Khan, A.S., Huang, S., 1992. Experimental and theoretical study of mechanical behavior of 1100 aluminum in the strain rate range 10–5–104s⁻¹. *Int. J. Plast.* 8, 397–424. [https://doi.org/10.1016/0749-6419\(92\)90057-J](https://doi.org/10.1016/0749-6419(92)90057-J).
- Khan, A.S., Liang, R., 1999. Behaviors of three BCC metal over a wide range of strain rates and temperatures: experiments and modeling. *Int. J. Plast.* 15, 1089–1109. [https://doi.org/10.1016/S0749-6419\(99\)00030-3](https://doi.org/10.1016/S0749-6419(99)00030-3).
- Klepaczko, J.R., 1994. An experimental technique for shear testing at high and very high strain rates. The case of a mild steel. *Int. J. Impact Eng.* 15, 25–39. [https://doi.org/10.1016/S0734-743X\(05\)80005-3](https://doi.org/10.1016/S0734-743X(05)80005-3).
- Klepaczko, J.R., Nguyen, H.V., Nowacki, W.K., 1999. Quasi-static and dynamic shearing of sheet metals. *Eur. J. Mech. A. Solids* 18, 271–289. [https://doi.org/10.1016/S0997-7538\(99\)80016-3](https://doi.org/10.1016/S0997-7538(99)80016-3).
- Krüger, L., Meyer, L.W., Razorenov, S.V., Kanel, G.I., 2003. Investigation of dynamic flow and strength properties of Ti-6-22-22S at normal and elevated temperatures. *Int. J. Impact Eng.* 28, 877–890. [https://doi.org/10.1016/S0734-743X\(02\)00151-3](https://doi.org/10.1016/S0734-743X(02)00151-3).
- Lindholm, U.S., 1964. Some experiments with the split hopkinson pressure bar. *J. Mech. Phys. Solids* 12, 317–335. [https://doi.org/10.1016/0022-5096\(64\)90028-6](https://doi.org/10.1016/0022-5096(64)90028-6).
- Marchand, A., Duffy, J., 1988. An experimental study of the formation process of adiabatic shear bands in a structural steel. *J. Mech. Phys. Solids* 36, 251–283. [https://doi.org/10.1016/0022-5096\(88\)90012-9](https://doi.org/10.1016/0022-5096(88)90012-9).
- Merle, R., Zhao, H., 2004. Experimental study of sheet metals under dynamic double shear at large strains. *Key Eng. Mater. Trans. Tech. Publ.*, 787–792.
- Meyer, L.W., Halle, T., 2011. Shear strength and shear failure, overview of testing and behavior of ductile metals. *Mech. Time-Depend Mater.* 15, 327–340. <https://doi.org/10.1007/s11043-010-9113-x>.
- Meyer, L.W., Krüger, L., 2000. Drop-weight compression shear testing. *ASM Handbook* 8, 452–454.
- Meyer, L.W., Staskewitsch, E., Burblies, A., 1994. Adiabatic shear failure under biaxial dynamic compression/shear loading. *Mech. Mater.* 17, 203–214. [https://doi.org/10.1016/0167-6636\(94\)90060-4](https://doi.org/10.1016/0167-6636(94)90060-4).
- Meyers, M.A., Staudhammer, K.P., Murr, L.E., 1986. *Metallurgical Applications of Shock-wave and High-strain-rate Phenomena*. Dekker.
- Meyers, M.A., Xu, Y.B., Xue, Q., Pérez-Prado, M.T., McNelley, T.R., 2003. Microstructural evolution in adiabatic shear localization in stainless steel. *Acta Mater.* 51, 1307–1325. [https://doi.org/10.1016/S1359-6454\(02\)00526-8](https://doi.org/10.1016/S1359-6454(02)00526-8).
- Nie, X., Chen, W.W., Sun, X., Templeton, D.W., 2007. Dynamic failure of borosilicate glass under compression/shear loading experiments. *J. Am. Ceram. Soc.* 90, 2556–2562.
- Peirs, J., Verleysen, P., Degrieck, J., 2012. Novel technique for static and dynamic shear testing of Ti6Al4V sheet. *Exp Mech* 52, 729–741. <https://doi.org/10.1007/s11340-011-9541-9>.
- Peirs, J., Verleysen, P., Degrieck, J., Coghe, F., 2010. The use of hat-shaped specimens to study the high strain rate shear behaviour of Ti-6Al-4V. *Int. J. Impact Eng. Impact Loading Lightweight Struct.* 37, 703–714. <https://doi.org/10.1016/j.ijimpeng.2009.08.002>.
- Peirs, J., Verleysen, P., Van Paepegem, W., Degrieck, J., 2011. Determining the stress-strain behaviour at large strains from high strain rate tensile and shear experiments. *Int. J. Impact Eng.* 38, 406–415. <https://doi.org/10.1016/j.ijimpeng.2011.01.004>.
- Pochhammer, L., 1876. Beitrag zur Theorie der Biegung des Kreiscylinders. *Journal für die reine und angewandte Mathematik* 81, 33–61.
- Ravichandran, G., Subhash, G., 1994. Critical appraisal of limiting strain rates for compression testing of ceramics in a split hopkinson pressure bar. *J. Am. Ceram. Soc.* 77, 263–267. <https://doi.org/10.1111/j.1151-2916.1994.tb06987.x>.
- Rittel, D., Lee, S., Ravichandran, G., 2002. A shear-compression specimen for large strain testing. *Exp. Mech.* 42, 58–64. <https://doi.org/10.1007/BF02411052>.
- Rusinek, A., Klepaczko, J.R., 2001. Shear testing of a sheet steel at wide range of strain rates and a constitutive relation with strain-rate and temperature dependence of the flow stress. *Int. J. Plast.* 17, 87–115. [https://doi.org/10.1016/S0749-6419\(00\)00020-6](https://doi.org/10.1016/S0749-6419(00)00020-6).
- Shi, F.F., Merle, R., Hou, B., Liu, J.G., Li, Y.L., Zhao, H., 2014. A critical analysis of plane shear tests under quasi-static and impact loading. *International Journal of Impact Engineering*, Advances in Impact Engineering: Selected papers from AEP2012 74, 107–119. <https://doi.org/10.1016/j.ijimpeng.2014.06.012>.
- VOCE, E., 1948. The relationship between stress and strain for homogeneous deformation. *J. Inst. Met.* 74, 537–562.
- Xu, Z., Ding, X., Zhang, W., Huang, F., 2017. A novel method in dynamic shear testing of bulk materials using the traditional SHPB technique. *Int. J. Impact Eng.* 101, 90–104. <https://doi.org/10.1016/j.ijimpeng.2016.11.012>.
- Xu, Z., Liu, Y., Sun, Z., Hu, H., Huang, F., 2018. On shear failure behaviors of an armor steel over a large range of strain rates. *Int. J. Impact Eng.* 118, 24–38. <https://doi.org/10.1016/j.ijimpeng.2018.04.003>.

- Zerilli, F.J., Armstrong, R.W., 1992. The effect of dislocation drag on the stress-strain behavior of F.C.C. metals. *Acta Metall. Mater.* 40, 1803–1808. [https://doi.org/10.1016/0956-7151\(92\)90166-C](https://doi.org/10.1016/0956-7151(92)90166-C).
- Zhou, T., Wu, J., Che, J., Wang, Y., Wang, X., 2017. Dynamic shear characteristics of titanium alloy Ti-6Al-4V at large strain rates by the split Hopkinson pressure bar test. *Int. J. Impact Eng.* 109, 167–177. <https://doi.org/10.1016/j.ijimpeng.2017.06.007>.
- Zhu, S., Guo, Y., Chen, H., Li, Y., Fang, D., 2019. Formation of adiabatic shear band within Ti-6Al-4V: Effects of stress state. *Mech. Mater.* 137. <https://doi.org/10.1016/j.mechmat.2019.103102> 103102.